Impact of Dissociation on Modeling for Plasma Aerocapture

Sara Emese Barczay

A thesis
submitted in partial fulfillment of the
requirements for the degree of

Master of Science in Aeronautics and Astronautics

University of Washington

2023

Reading Committee:
Justin Little, Chair
Uri Shumlak

Program Authorized to Offer Degree:
William E. Boeing Department of Aeronautics and Astronautics

University of Washington

Abstract

Impact of Dissociation on Modeling for Plasma Aerocapture

Sara Emese Barczay

Chair of the Supervisory Committee:
Assistant Professor Justin Little
William E. Boeing Department of Aeronautics and Astronautics

Interplanetary missions require changes in velocity to travel along planned trajectories, make course corrections, and for planetary capture. When performed using traditional propulsive methods, the mass and monetary costs increase exponentially as the total sum of the necessary velocity change increases. Magnetoshell Aerocapture (MAC) is an experimental technology that has mission-enabling potential, especially for the outer edges of the solar system, mainly because it reduces the costs associated with creating the changes in velocity needed for orbital insertion, through reductions in mass. It works by entraining the neutral population from the atmosphere within a plasma dipole. Through this transfer of mass and energy, the momentum of the neutrals is transferred to the spacecraft, effectively creating a drag force. Previous models for MAC have explored the plasma chemistry reactions within this process, and the resulting power transfer for ionization and charge exchange, where four populations (ions, electrons, stream neutrals, and secondary neutrals) were considered. Here an expanded model is presented where dissociation is additionally considered and the resulting seven populations are included. Results show that the inclusion of dissociation expands the amount of power being captured from the neutral atmospheric stream by the dipole. Additionally, at lower temperatures, there is a secondary peak power transfer within the system. Together, these findings imply that previously determined regions of operation within a planet's atmosphere for a spacecraft using MAC could be more extensive than expected.

TABLE OF CONTENTS

LIST OF FIGURES

LIST OF TABLES

ACKNOWLEDGMENTS

This Thesis would not have been possible without the help and support of many people. I am incredibly thankful for the opportunity given to me by my advisor, Professor Justin Little, to participate in research within the SPACE Lab. I would not have been able to complete this work without his steady patience, guidance, and support. I am thankful to both Justin and Professor Uri Shumlak for being excellent and compassionate teachers. Much of this work is based on Charlie Kelly's. His willingness to sit with me as a new graduate student to make sure I understood his research ensured a solid foundation on which to build my own. The camaraderie and support within the plasma group have been exemplary. I feel fortunate to have gone through this experience with this caliber of people. Special thanks are owed to Bennett Diamond, Peter Thoreau, Arvindh Sharma, and Landon Bevier.

I first came to UW as an undergraduate in the ME Department. Alberto Aliseda took me on as an undergraduate research assistant and has allowed me to continue growing as a researcher in his lab throughout my time at UW. His advice and mentorship have gotten me through difficult periods. I owe a deep debt of gratitude to him and the staff and researchers in ME who encouraged me on this path and have continued to support me in my graduate work, especially Kendra Burdett, Wanwisa Kislang, Eamon McQuaide, and Bill Kuykendall.

I am thankful to the fencers and coaches at the SAS Fencing Club, especially Eric Piispanen, and Nikita Sakhanenko, for providing excellent examples of leadership and a creating community from which to draw strength. Finally, my friends, parents, and family have been extremely patient with me while I've restructured my life around engineering. I would not be here without their support in this endeavor, especially my parents, George and Katalin Barczay, sister, Nora Barczay, and friends Alex Swan, Rebecca Alvarez, and Laurel Marsh.

DEDICATION

For
George Tibor Bárczay
and
Éva Bárczay-Miller

Chapter 1

INTRODUCTION

Orbital insertion maneuvers are required for planetary capture. To perform them, a change in velocity ΔV is applied to decelerate the spacecraft and change its trajectory from hyperbolic to elliptical or circular. The amount of ΔV needed to complete a maneuver is dependent on the spacecraft's entry velocity and the desired resulting orbit. Traditionally, ΔV is created using chemical burns resulting in propulsive insertion. This method requires transporting the mass needed for the burn to the final destination. Reducing or eliminating this mass could free up space for additional science, and create cost savings through mass savings. Therefore, alternative methods to chemical insertion, such as aerobraking, aerocapture, and solar electric propulsion are being investigated and implemented, and in some cases have already been used [1][2][3][4].

Aerocapture is a theoretical orbit insertion maneuver. During aerocapture ΔV is applied to the spacecraft by a single pass through the target planet's atmosphere. This is done through either lift modulation, where the geometry of the spacecraft is used to change the angle of the spacecraft to adjust its trajectory, or through drag modulation, where the area of the spacecraft is changed to create a deceleration event and change its trajectory. NASA [5][1][6], ESA[7], JAXA[8], and various other national space organizations have researched the efficacy and feasibility of aerocapture and aerobraking for decades. Studies show that the implementation of aerocapture over traditional methods would result in significant cost and mass savings while shortening trip times and reducing risk because aerocapture inherently requires an in situ utilization of the atmosphere[9][10][11]. In many cases, this allows for a significant reduction in the amount of fuel needed for a mission. The savings generated by using aerocapture over other propulsive methods open up mission possibilities that would otherwise be prohibited by large costs or low returns[9]. While components of aerocapture have been successfully tested, a full-scale test has yet to be conducted, making lack of heritage one of the biggest drawbacks of aerocapture, despite its potential benefits.

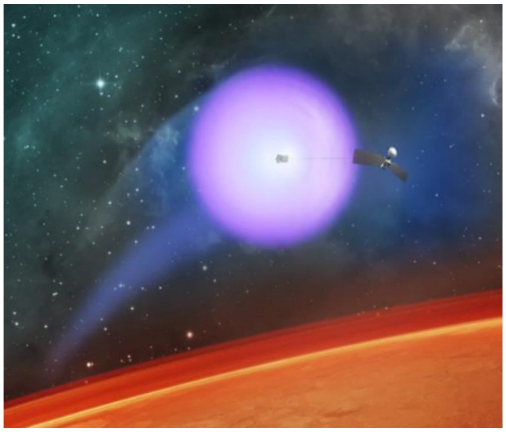

Figure 1.1: Artists rendition of Magnetoshell Aerocapture[3].

Magnetoshell Aerocapture (MAC) is a continuously variable drag-modulated type of aerocapture. Like other drag-modulated aerocapture, MAC creates drag by changing its effective area, but instead of using a mechanical or physical architecture, it utilizes a plasma dipole. As the spacecraft enters the atmosphere, the plasma dipole entrains neutral atoms and molecules, which through collisional processes with the plasma, impart a drag force onto the craft. Figure 1.1 shows an artist's interpretation of MAC, with the plasma dipole trailing behind the spacecraft, entraining neutrals as it passes through the atmosphere of a planet. Like traditional aerocapture, MAC maintains mass and cost savings by using less fuel[12][3][4][13]. These savings are amplified because the MAC architecture is lighter than that of traditional aerocapture. Additionally, because it is a drag-modulated device, MAC provides more control in the capture process which can serve to lower risk.

So far, most work on MAC has focused on modeling the plasma chemistry of reactions with the largest cross sections for a single species[12][3][14][15]. These models provide an analytical framework to explore the interactions generating drag in MAC. Some experimental campaigns have been run[12][3][16], which have validated that the interaction between a neutral stream and plasma dipole generates drag. Together, the results from the analytical and experimental work support the concept of MAC as a cost-saving, mission-enabling device.

The present work seeks to broaden our understanding of the interaction between the neutral stream and the plasma dipole by implementing an analytical model which expands both the number of species being considered as well as the number of reactions. How these components transfer mass and kinetic energy from the neutral stream to the dipole will be explored. Past efforts have focused on electron impact ionization and charge exchange as the main drivers of mass and power captured within MAC. Here, electron impact dissociation is additionally included. This means that the number of species included expands to seven: $H_{2,sn}, H_{2,nd}, H_{2+}, H_{sn}, H_{nd}, H+$, and $e-$. The sn subscript represents the stream neutrals, while the nd represents the secondary neutrals formed after interaction with the plasma dipole. Furthering our understanding of these interactions and how power is initially captured into the MAC moves us closer to the implementation of this technology.

This thesis will first provide additional background on both traditional aerocapture and MAC. The equations and assumptions for the model will then be enumerated, followed by the method of implementation and specific values used. Results will then be presented, analyzed, and placed into the larger context. Finally, future work will be presented.

Chapter 2

BACKGROUND

2.1 Mechanics of Flight and Orbit Insertion

Traveling to destinations outside of Earth requires changes in velocity. The sum of the changes in velocity ΔV needed to accelerate through launch, complete intermediary trajectory maneuvers, and orbit insertion at the final destination is the total ΔV for a mission [17]. When considering reaction mass propulsion, like chemical propulsion, this ΔV is governed by the Tsiolkovsky Rocket Equation:

$$\Delta v = v_e ln \frac{m_0}{m_f} \tag{2.1}$$

Here, m_0 is the initial mass, m_f is the mass after the maneuver is completed, and v_e is the effective exhaust velocity. The initial mass of the rocket grows exponentially as the ΔV of a mission increases. Generally, exploration further from Earth requires increasing ΔV, and thus the mass and cost of a mission. Since increases in mass correspond to increases in cost and therefore less mass allocation to payloads, and since there is interest in exploring the edges of the solar system, there is an incentive to investigate methods outside of reaction mass propulsion with which to perform the necessary ΔV maneuvers. Aerocapture, and its associated technologies, are one alternative being explored.

2.2 Traditional Aerocapture

Aerocapture was first proposed in 1969 by London as a means for changing the orbital parameters of satellites [18][11]. Its in-situ utilization of a planet's atmosphere allows for a reduction in the cost of missions from mass savings because it becomes unnecessary to transport the reaction mass needed to create the ΔV for orbit insertion. Aerocapture also allows for shorter trip times, because increases in approach velocities necessitating a higher ΔV, do not also need the corresponding increase in mass.

Figure 2.1 depicts the aerocapture process. The spacecraft enters into an intercept trajectory along the orange line. As it approaches the body, its speed increases. Aerocapture is performed along the red line as the spacecraft dips down into the atmosphere of the planet. The ΔV needed to transition from the parabolic to elliptical orbit is applied during this phase of flight. The duration of the maneuver and how it is performed depends on the desired ΔV and the type of aerocapture being performed. In the blue post-exit region, the spacecraft moves along its new elliptical orbit. If it were to continue on this orbital path, it would pass through the atmosphere of the planet again, so a final periapsis raise is completed to adjust the orbit and place the spacecraft into its final elliptical postcapture orbit along the green line [10].

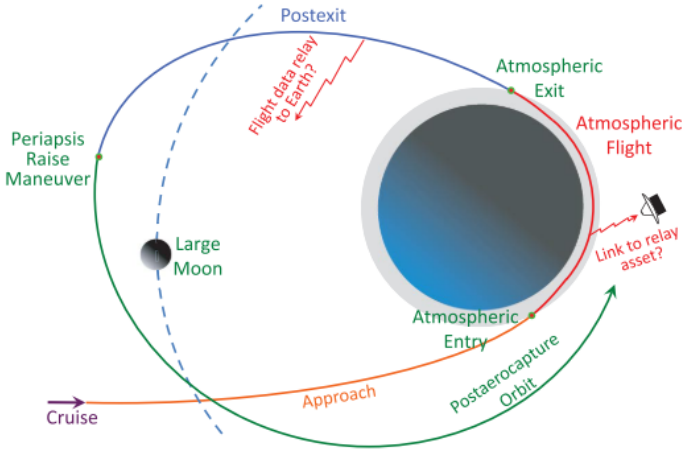

Figure 2.1: The spacecraft enters into the planet's sphere of influence along the orange line, performs the aerocapture maneuver along the red, and then exits onto the blue line. Finally, a stable orbit is reached along the green line [10].

In Figure 2.1 colors of the depicted orbital path for aerocapture coincide with a risk assessment performed by Spliker et al. Little additional knowledge is needed to execute the cruise (purple), post-exit (blue), and post-capture orbit (green) sections of the aerocapture maneuver. In the approach (orange) and atmospheric flight (red) areas of flight, analysis indicates that risk reduction actions in the form of additional research and test should be completed for aerocapture to be completely flight ready.

Aerocapture maneuvers use either lift modulation or drag modulation to complete orbit insertion. In the former, control surfaces such as flaps are used to exert influence on the bank angle of the spacecraft to modulate its energy and thus trajectory as it passes through the atmosphere [19][20]. The parameter used to quantify the shapes of these types of vehicles is their Lift to Drag ratio or L/D. Vehicles with low L/D ($L/D \leq 0.4$) have been utilized in flight in non-aerocapture scenarios and contain a significant amount of heritage. Mid-L/D ($L/D = 0.6 - 0.8$) have also been utilized but with less frequency [21].

Drag-modulated aerocapture has not been as widely used. Instead of working with the L/D of the vehicle, drag modulation aerocapture works to control the vehicle's ballistic coefficient. [19]. The ballistic coefficient is defined as:

$$\beta = \frac{m}{C_D S_{ref}} \tag{2.2}$$

Here, m is the mass of the craft, C_D is the coefficient of drag, and S_{ref} is the reference area. This ratio describes the relationship between inertial and drag forces[22]. In drag-modulated aerocapture, the denominator of this ratio, the effective drag area, is changed, typically in the form of a deployable device.

While not strictly aerocapture, aerobraking is a closely related maneuver that bears noting, especially since it is a heritage technology, while aerocapture is not. Aerobraking differs from aerocapture in that it utilizes multiple atmospheric passes for orbit insertion instead of a single one. Until the early 1990s aerobraking and aerocapture were used interchangeably [11]. Since then literature has differentiated between the two maneuvers. In aerobraking passes are completed higher in the atmosphere of the planet. This means that the thermal loads and dynamic pressures on the spacecraft tend to be smaller than those acting on the spacecraft during aerocapture maneuvers. While aerocapture has not yet been performed, aerobraking maneuvers have been completed since the early 1990s by NASA (Magellan, Venus Express, Mars Global Surveyor, Mars Reconnaissance Order)[10], ESA (ExoMars Trace Gas Orbiter)[7], and JAXA (HITEN)[8].

While it has not yet been flight tested, since its inception, there have been over 350 published investigations into the application of aerocapture and its related technologies.

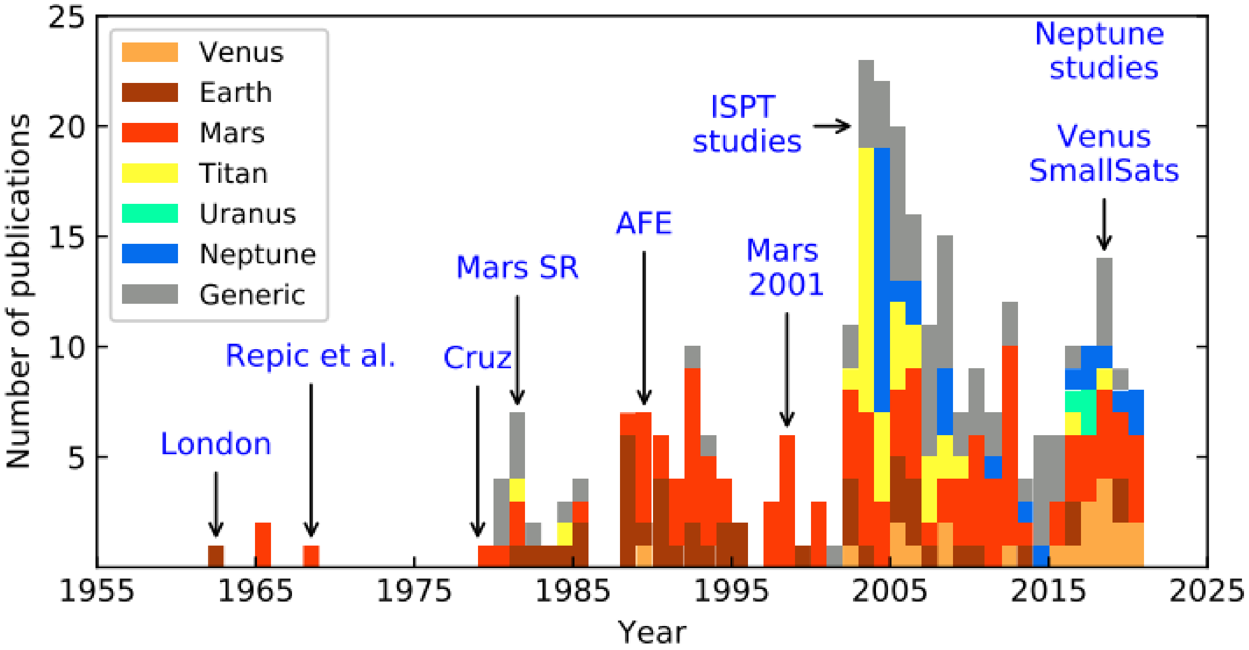

Figure 2.2: Publication record of aerocapture-related literature by target destination [11].

These are displayed graphically by their target destination in Figure 2.2. A marked increase in the number of studies done can be seen in 2005, with the publication of NASA's In-Space Propulsion Technology Program (ISPT), which placed aerocapture as one of its central aims. In the same year, NASA indicated an interest in exploring the Ice Giants, resulting in a corresponding jump in aerocapture publications to that destination [20]. Interest in the Ice Giants as potential candidates for aerocapture has continued since then, as has an interest in Mars and Venus.

In 2005, Hall et al. completed an exhaustive cost-benefit analysis of available orbit insertion technologies. To do this, they compared chemical propulsion, solar electric propulsion, and aerobraking, to aerocapture for 11 robotic missions at 8 different destinations. These technologies are inherently disparate in their composition, so the analysis focused on finding unifying ways in which to create direct comparisons. The authors achieved this by quantifying the overall cost of a mission as well as the mass savings. They found that aerocapture overwhelmingly creates both cost and mass savings, the magnitudes of which vary depending on the destination [9].

Figure 2.3 summarizes the findings related to cost benefits by comparing the cost of an aerocapture to the next most cost-effective orbit insertion method between aerobraking, chemical propulsion, and solar-electric propulsion. Most significantly using non-aerocapture methods, the cost per kilogram for the Saturn S1 and Jupiter J1 missions are prohibitively high, making aerocapture an enabling technology for those cases. Aerocapture significantly outperforms the next-best non-aerocapture alternative at Neptune N1, Uranus U1, and Titan T1. For these, utilizing aerocapture would save between 0.7 and 1.5 million dollars per kilogram. Cost savings per kilogram are small to negligible for the both Venus (V1 and V2) missions and both Mars (M1 and M2) missions explored. The only place where aerocapture is more expensive than non-aerocapture is the Jupiter J2 mission.

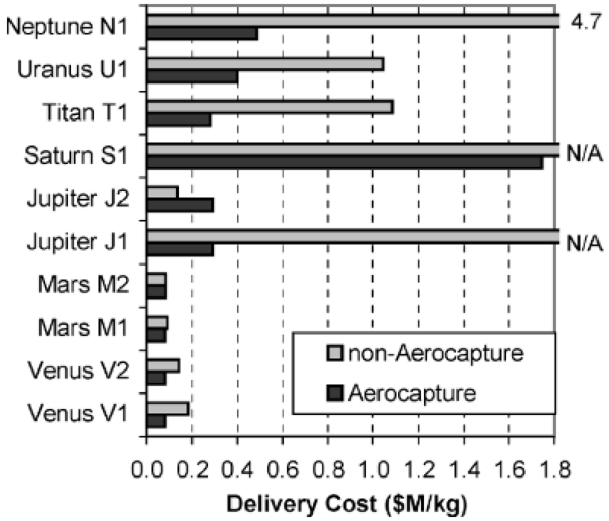

Figure 2.3: Cost comparison of Aerocapture to next most cost-effective method for a mid-sized launch vehicle. [9].

Figure 2.4 summarizes key findings with regard to mass. Similar to the cost savings the largest mass savings appear for the Ice Giants (N1, U1) and Titan T1, where the percent increase in the final amount of delivered mass ranges between 823% and 218%. The percent increase in mass is more modest comparatively at Venus V1, but not insignificant, and small at Mars M1 and M2. A percent increase of infinite for Jupiter J1 and Saturn S1, where aerocapture is an enabling technology. The trends in mass savings largely scale with ΔV. In cases, like Mars, where a low ΔV is needed, or the orbit insertion is less complicated, the mass benefits of aerocapture do not carry through. The negative mass benefit in Jupiter J2 is attributed to the large aeroshell needed to protect the spacecraft from high temperatures

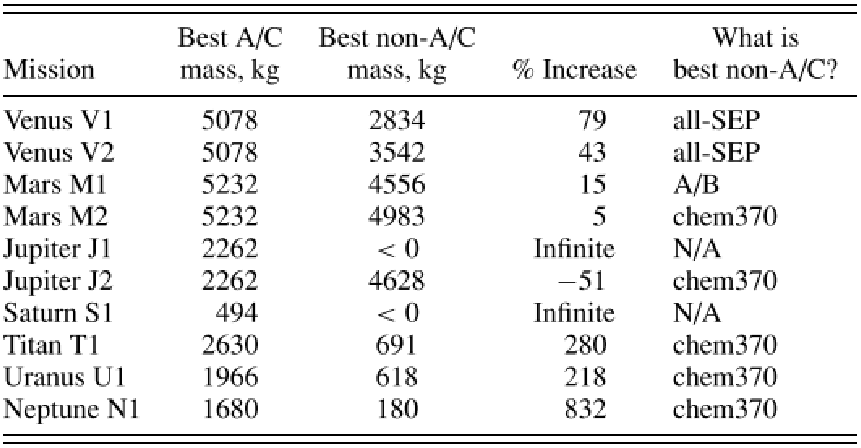

Mission	Best A/C mass, kg	Best non-A/C mass, kg	% Increase	What is best non-A/C?
Venus V1	5078	2834	79	all-SEP
Venus V2	5078	3542	43	all-SEP
Mars M1	5232	4556	15	A/B
Mars M2	5232	4983	5	chem370
Jupiter J1	2262	< 0	Infinite	N/A
Jupiter J2	2262	4628	-51	chem370
Saturn S1	494	< 0	Infinite	N/A
Titan T1	2630	691	280	chem370
Uranus U1	1966	618	218	chem370
Neptune N1	1680	180	832	chem370

Figure 2.4: Comparison of additional mass made possible by the use of Aerocapture. [9].

and pressures resulting from high entry velocities; even though this mission saves on fuel, the mass difference cannot be made because the overall ΔV is small.

Hall's assessment focused largely on providing an analysis of the cost and mass savings. However, there are many components, in different stages of mission readiness, that makeup aerocapture. A NASA Technology Overview defined the aerocapture aspects of a mission to include: guidance and navigation modeling, atmospheric modeling, aero-heating, thermal protection systems, aeroshell structure and design, mass properties analysis, and spacecraft design [5].

Studies completed since Hall et al. initial assessment have largely supported their central findings. Namely, aerocapture is a mission-enabling technology for the ice giants, and overall, it represents significant cost savings for most missions over other orbit insertion methods. Current work relevant to aerocapture has focused on the application of aerocapture to small satellites [23], related enabling technologies such as improving density modeling[19], or the ways in which the development of new TPS materials could broaden where aerocapture can be practically applied[1][24]. Most recently, a white paper by Dutta et al. makes the argument that aerocapture has become feasible at the Ice Giants even with the large thermal loads and dynamic pressures because of significant advances in TPS materials [25]. They additionally focus on the ways in which current orbital insertion methods, like aerobraking, which are comparatively more complex have been successfully implemented, implying that aerocapture as a less complex maneuver, should be possible to implement successfully.

2.3 Plasma Aerocapture

Plasma aerocapture is a subcategory of aerocapture where the traditional hard shell is replaced by a plasma dipole, creating a magnetoaeroshell. Since Kirtely et al. suggested and Kelly et al. analytically demonstrated that the size of the magnetoshell can be continuously varied (CV), it additionally falls underneath the category of continuously-variable drag-modulated aerocapture. Broadly, MAC functions by entraining atmospheric neutrals into a magnetically confined plasma. The neutrals are captured as interaction with the plasma turns them into ions. Once captured, the neutrals transfer their momentum to the spacecraft via the magnetic field lines to create drag.

While significant technological advances have made the implementation of traditional aerocapture theoretically feasible at more locations[25], its execution still involves high heat loads and dynamic pressures because it requires diving deep into a planet's atmosphere [24]. Plasma aerocapture could help mitigate these risks since it can be implemented at higher altitudes relative to traditional aerocapture. Additionally, its ability to modulate the amount of drag produced makes plasma aerocapture well-suited to mitigating risks associated with insertion at planets where there is a lack of knowledge available on the planet's atmosphere [3][12][14][15] .

Figure 2.5 shows how a CV drag aerocapture device functions. As with other drag-modulated devices, insertion depends on the ballistic coefficient β. In single or multiple-stage drag modulation aerocapture devices, the craft enters the atmosphere at an initial β_1 and deploys drag devices to create a change in acceleration and exits at a final β_2. This is in contrast to CV drag devices where the β value can range between β_1 and β_2 as it moves through the atmosphere. The ability of CV devices to modulate their β value means that CV drag devices have inherent risk mitigation built into their structure because they are able to

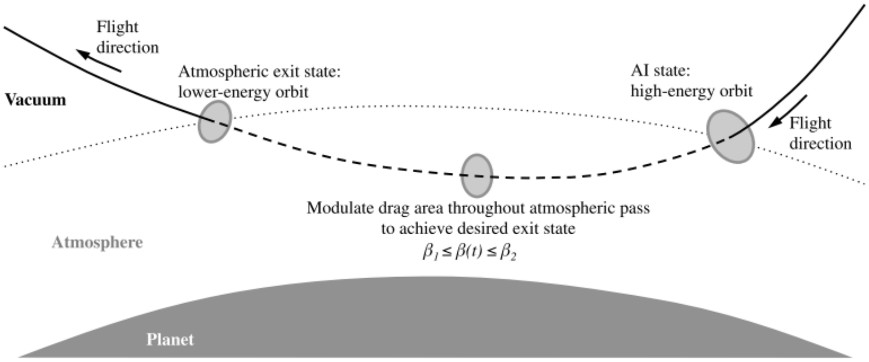

Figure 2.5: In CV Drag Aerocapture, the effective area of the spacecraft is varied. [22].

adapt to potentially unseen circumstances [22]. In the single and multi-stage devices, there is more risk because they are comparatively less able to adapt to potential issues since there are only minimal ways in which to vary their β coefficient. In MAC, the β value is related to the amount and mass of neutrals entrained by the plasma dipole, the entry velocity of the vehicle, and the effective area over which the dipole acts.

While a full plasma aerocapture device has not yet been constructed, theoretical work has been completed on modeling plasma aerocapture, and some experimental campaigns have been run for concept validation. Slough et al. were the first to propose the concept of MAC [2]. Building on the concept of a Magnetic Sail, they proposed a high β_p plasma aeroshell which would encapsulate the spacecraft, both protecting the spacecraft and providing a drag modulation device. Note that this β_p is distinct from the ballistic coefficient previously discussed. Here β_p refers to the ratio of the plasma pressure to the magnetic pressure, as defined below:

$$\beta_p = \frac{n k_B T}{B^2/2\mu_0} \tag{2.3}$$

In their design, a rotating magnetic field is produced using a pair of polyphasic coils, which drives the necessary current for the plasma to inflate and then maintain a large-scale magnetic structure. Definitions for the drag force on the spacecraft and a basic parameter scaling for the plasma magnetoshell are laid out. The authors identify three conditions for the MAC to be effective. First, the local atmospheric drag on the spacecraft needs to be small.

Second, the scale of the MAC during the maneuver must be on the same order of magnitude as the mean free path for the dominant reaction, which they identified as charge exchange. Finally, the strength of the magnetic field must be such that the charge exchange collisional frequency must be less than the ion cyclotron frequency. The first of these conditions relates to the inflation of the high β plasma, while the latter two conditions work to ensure that the newly created ions are captured long enough for them to transfer their momentum to the spacecraft and thus produce drag. By applying the parameter scaling, Slough et al. find that the drag force scales with magnetoshell size and plasma density. These preliminary findings are echoed throughout all successive studies.

Kirtley et al. builds on Slough et al.'s work by developing additional equations for a transient analytical model, performing a MAC mission design and analysis for Mars and Venus, and running an experimental campaign for a Phase 1 project[3]. In a deviation from Slough et al., Kirtley et al. makes the determination that a high-β plasma is not necessary for successful mass and energy capture. Since a low-β dipole plasma is easier to create, model, and maintain during flight, subsequent models and designs assume a low-β configuration.

Kirtley et al.'s 2D transient model provides insights into the interaction between the neutral stream and plasma dipole, past initial parameter scaling. For this model, they assume a cylindrical geometry, uniform azimuthal plasma, uniform neutral flow, a cubic radial fall-off for the initial density distribution on the plasma, and a fixed magnetic field. They employ equations for density, diffusion, and heating, and propagate them over different time scales to demonstrate the relaxation of electron and ion temperature to a steady state. Their results indicate that the ion temperatures will equilibrate to the average temperature of the incoming flow, while the electron temperature will find an equilibrium at a value lower than the ion temperature. They find that the equilibrium ion density depends on both the temperature of the incoming flow and the diffusion rate.

These models are then applied to the specific cases of Mars and Neptune to predict the drag across a variety of design parameters to choose the most appropriate set. Their final design at Neptune resulted in a MAC system weighing 207kg, as compared to an

885kg traditional aeroshell which increased the dry payload fraction by 8%. At Mars, they estimated that using MAC would result in 224 MT of mass savings, resulting in total cost savings on the order of $2 Billion.

Figure 2.6 displays the plasma magnetoshell experiment run by Kirtley et al. during Phase 1. They used a 200-turn magnet with a two-phase spherical RF antenna. A stationary magnetoshell was observed when the high-velocity jet impinged on the magnet. The thrust stand recorded a corresponding force of 220mN which they calculated to represent a relative drag increase of 1150 over the case without the magnetoshell on.

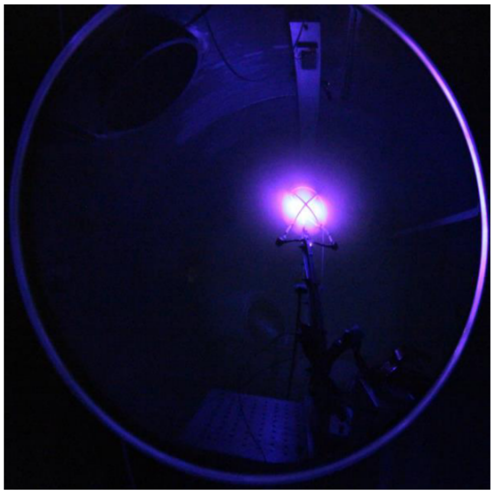

Figure 2.6: Magnetoshell formed during Phase 1 testing by accelerating a high-velocity argon jet at a magnetic dipole[3].

Kirtely et al. continued their work in a Phase 2 project [12]. Expanding on their Phase 1 work, they proposed a design to build a MAC and test it by launching from the ISS. Their final design included a standard copper electromagnet containing a total of 210 turns, to produce a center field strength of 0.0172 T. Its total mass, including the PPU system is estimated to be 4 kg. A proxy to the designed magnetoshell was tested to quantitatively validate the concept. Figure 2.7 displays the experiment in progress. With the magnet off on the left, a small amount of propellant can be seen. When the magnet is turned on the right, a large dipole field is formed and expands, confirming its functionality.

Throughout the two phases of funding for MAC Kirtley et al. developed a transient analytical model, performed mission studies for MAC at Mars, Venus, and Earth, and designed a MAC device for a 6U cubsat to be launched from the ISS for testing. From these analyses, they showed that drag can theoretically be produced with MAC, and that compared to traditional aeroshell devices, MAC represents significant mass and cost savings, as well as reduced risk. They also ran two experimental campaigns. In the first, they demonstrated that a neutral beam impinging on a magnetic dipole will cause measurable drag. In the second, they tested an injector system to show that a magnetoshell will expand around a stationary magnetic dipole.

Figure 2.7: Phase 2 testing displayed that when the magnet was turned on (right) a magnetoshell would form and expand about the injected gas. Left shows the magnet off for comparison [12].

Hancock et al.[26] implemented the model developed by Kirtely et al. to further investigate the application of MAC at Mars. They explored additional magnet sizes as well as the sensitivity of the system. Their analysis confirmed that MAC systems are capable of providing the needed ΔV to perform orbit insertion maneuvers at Mars. They additionally demonstrated that the largest mass driver within the MAC system is the magnet itself and that the design requirements for the size of the magnet increase quickly with the altitude at which the MAC maneuver is performed. Higher altitudes require stronger and thus heavier magnets because the atmosphere is less dense. To achieve an equivalent amount of drag needed at a lower and more dense altitude, a larger magnet creates a greater effective area for the magnetoshell to capture neutrals. This shows that in designing a MAC system, there is a mass trade-off between the mass of the magnet and the amount of TPS materials needed since lower altitudes require smaller magnetoshells to create the equivalent drag, but more protection from thermal loading, and thus more mass.

Kelly et al. were the first to derive a self-consistent model for the plasma dipole from first principles incorporating both mass and energy conservation [4]. In their model, they consider both ionization and charge exchange reactions with the neutral stream at a fixed density.

Using this model, they are able to provide a more detailed method for calculating drag. The approach used by Kelly et al. allows for a more detailed accounting of the mass and energy transfer than the models developed by Slough et al. and Kirtely et al. because they consider the global interactions together instead of extending the physics of a single particle to the global case. Through their analysis, Kelly et al. find that there is a trapping region within which ions are created through interaction with the neutral stream and contribute to the mass and energy of the plasma. Outside of this region, particles are deflected. They additionally find that ingested mass scales with both the magnetic field strength and the neutral stream density, demonstrating that MAC can be used as a drag-modulating device.

In further work, Kelly et al. include a 1D model of the neutral stream to more accurately determine the transfer of mass and energy [13]. Critically, this model revealed the existence of three separate operating regimes for the interaction between a neutral stream and plasma dipole. Transitions between the regimes depended on the neutral stream velocity. Since the neutral stream velocity is representative of the spacecraft approach velocity, and since not all of the regimes were able to produce a self-sustaining plasma, this set limits on the types of missions where MAC can be applied. The expanded model is used to determine how drag scales with MAC parameters and to find flight envelopes for MAC use at Venus, Mars, Saturn, and Neptune. Kelly et al. find that the amount of drag produced by the interaction between the neutral stream and the plasma dipole increases with plasma density and magnetic field strength. The latter dependence is important because a stronger field strength also means a larger effective area. Given the ballistic coefficients' dependence on area, this further confirms that MAC can be a continuously variable drag device by modulating the magnetic field strength. Analysis of the flight envelopes shows that MAC is possible at Saturn, Neptune, and Venus, but not at Mars because the lower velocities needed for orbit insertion are outside of the operating conditions for MAC.

Little et al., develop a more detailed model for exploring the mass and energy transfer of the neutral stream to the plasma dipole[14]. They first solve for the steady-state neutral stream density within the control volume. Then, they incorporate these solutions into the steady-state continuity and energy equations, which are then combined to find the total power balance within the control volume. Mode transition locations are identified within the power balance in terms of effective ionization energy and electron/ion confinement times. Understanding how the transitions between different regimes are dependent on what is physically happening within the plasma provides additional insight into the operating regimes of MAC. This model deviates from previous work in its treatment of how the plasma density scales with respect to the magnetic dipole. Instead of using a scaling with the magnetic field strength, they choose to scale based on the magnetic flux function.

Kelly et al. expand on the model for MAC by coupling the equations for the stream neutrals found in [14] with expanded continuity and energy equations for the ions, electrons, and secondary neutrals to create a global model which accounts for the physics of the system in a more detailed manner[15]. Unlike in [14], the equations are time-resolved instead of steady-state. They run the model with Argon to find how the temperature and density of the electrons, ions, and secondary neutrals evolve over time. Their results confirm the existence of three different operating regimes for MAC previously identified in [14].

The most recent work on MAC was an experimental campaign executed by Kelly et al. where a high-velocity neutral beam was accelerated and impinged upon a stationary magnetic dipole [16]. They observe that when the neutral beam interacts with the plasma dipole, its density and temperature increase. By invoking a power balance, they are able to show that there is a transfer of energy from the neutral beam to the plasma dipole. Limitations on test facilities prevented operation in regimes that would have directly validated exactly how the energy is being transferred. While they were unable to resolve the transfer of momentum to demonstrate how drag is created by the interaction, the results produced indicate that there is an effect, which with further testing and more sensitive instrumentation could be observed.

Overall, these studies indicate that MAC maintains the benefits of the traditional aerocapture structure discussed in the previous section in terms of mass and correlated cost savings. Since its structure is lighter than traditional aerocapture devices, these savings are amplified. Additionally, with MAC, there is less of a need to dive deeper into the atmosphere as compared to traditional aerocapture since the necessary densities for capture exist at higher altitudes, reducing the intensity of frictional heating ao the need to allocate mass to TPS. MAC's ability to function at higher altitudes coupled with its capacity to continuously modulate the drag make it a lower-risk orbit insertion method.

The following chapters will continue to build on the analytical work completed by Little et al. and Kelly et al. Their global models self-consistently solve for the transfer of mass and energy with a single species where the charge exchange and ionization reaction rates are considered. Here, these models will be extended to include electron impact dissociation into the continuity equations for the neutral stream to more accurately account for the physics involved in the power transfer of the neutral stream to the plasma dipole.

Chapter 3

PLASMA AEROCAPTURE MODEL

To determine the impact of including dissociation in the model between the neutral beam and plasma dipole, an analytical model is presented for the cases with and without dissociation. First, the model geometry is presented including general assumptions and the control volume definition. Then equations and specific assumptions for the case without dissociation and with dissociation are laid out. Chapter 4 details the implementation method in Mathematica for the equations developed in this chapter and includes the values used in the calculations.

3.1 Model Geometry

The magnetic field is defined in cylindrical coordinates (r, θ, z) following Jackson [27], as a loop current centered at the origin with a radius r_c and center magnetic field strength of B_0. The field is assumed to be uniform in θ, and low-β. In the equations below, Ψ is the magnetic flux function, K and E are the complete elliptic functions of the first and second kind respectively, and κ is included for simplification purposes.

$$\mathbf{B} = \frac{1}{r}\hat{e}_\theta \times \nabla\Psi \tag{3.1}$$

$$\Psi = \frac{2B_0 r_c^2 r}{\pi}\frac{\left(2-\kappa^2\right)K(\kappa^2) - 2E(\kappa^2)}{\kappa^2\sqrt{\left(r_c^2+r^2\right)+z^2}} \tag{3.2}$$

$$\kappa^2 = \frac{4rr_c}{(r+r_c)^2+z^2} \tag{3.3}$$

Figure 3.1 displays a cross-section of the magnetic field [15]. The neutral stream is shown impinging on the dipole along the z-axis. As it approaches the dipole from infinity, the stream has a uniform density n_∞ and velocity u_∞. The relevant control volume and surfaces

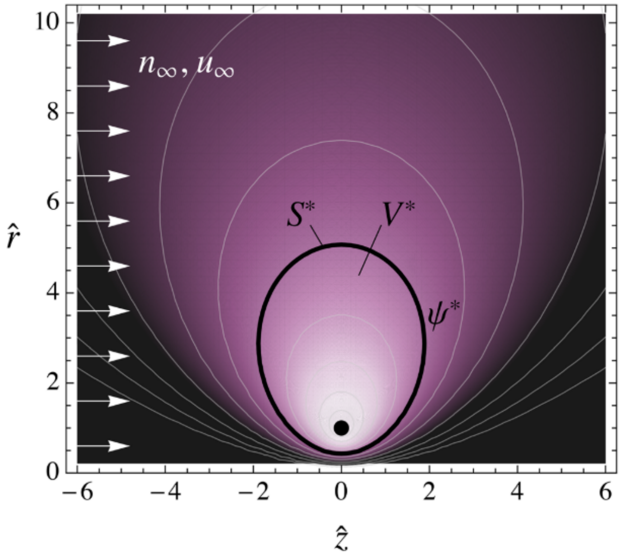

Figure 3.1: The neutral flow, n_∞ impinges on the plasma dipole with a velocity of u_∞. V^* the relevant volume considered, while S^* and Ψ^* are the corresponding surface and flux enclosing that volume[15].

considered are denoted by $*$'s. Following the derivations completed by Little and Kelly [14][15], the boundary of the control volume is given by:

$$\Psi^* = \sqrt{2\rho_L} \tag{3.4}$$

Ψ is the magnetic flux function shown above. ρ_L is the characteristic Larmor radius normalized by the magnet coil radius. Then, V^* is the volume encapsulated by Ψ^* and S^* is the surface of that volume. The control volume will increase with magnetic field strength and magnet coil radius. It will decrease if the mass of the ion species becomes heavier, or if the stream velocity increases.

$$\rho_L = \frac{m_i u_\infty}{eB_0 r_c} \tag{3.5}$$

3.2 Plasma Aerocapture without Dissociation

3.2.1 Continuity Equation

Stream neutral density is derived from the continuity equation following the processes and assumptions laid out in [14]. The general form of the continuity equation is:

$$\frac{\partial n_j}{\partial t} + \nabla \cdot (n_j \mathbf{u_j}) = \sum_s \dot{n_j^s} \tag{3.6}$$

The first term on the left-hand side represents the change in the species' density over time. Since a steady state is assumed, this term reduces to zero. The second term on the left hand side represents the flux of species across space. We assume that the stream has a uniform velocity and only acts in z with respect to the plasma dipole, reducing this term to a partial derivative with respect to z only, with the velocity represented as a constant u_∞. The right-hand side represents the sum of all sources and sinks for the neutral stream density and is quantified here through the reaction rates considered. For the case without dissociation, both electron impact dissociation and charge exchange reaction rates are included and represent sinks for the stream neutral density. There are no sources for the neutral stream within the control volume. Neutrals created by the interaction between the neutral stream and the plasma are regarded as a separate secondary neutral population. Considering the case for H2 with a single ion species, these simplifications and specifications result in:

$$\frac{\partial n_{sn}}{\partial z} = \frac{-R_{cx} n_{sn} n_e}{u_\infty} - \frac{R_{iz} n_{sn} n_{H2+}}{u_\infty} \tag{3.7}$$

Here, the subscript sn refers to the stream neutrals. Without dissociation, the application of charge neutrality ($n_{H2+} = n_e$) allows for further simplification, making the equation easier to solve.

$$\frac{\partial n_{sn}}{\partial z} = -\frac{R_{cx} + R_{iz}}{u_\infty} n_{sn} n_e \tag{3.8}$$

The equation is closed using an assumption on the scaling of the electron density with respect to the magnetic flux, where the subscript r is a reference location as defined below and $\alpha = 4$.

This assumption ties the density of the electrons to the magnetic flux and has been previously used as an approximation in strongly confined plasmas.

$$\frac{n_e}{n_{e,r}} = \left(\frac{\Psi}{\Psi_r}\right)^{\alpha} \tag{3.9}$$

Substituting this gives the final form of the continuity equation for the case considered:

$$\frac{\partial n_{sn}}{\partial z} = -\frac{R_{cx} + R_{iz}}{u_\infty} n_{sn} n_{e,r} \left(\frac{\Psi}{\Psi_r}\right)^{\alpha} \tag{3.10}$$

3.2.2 Power Captured

As the neutral stream interacts with the dipole, the molecules are captured at a rate equal to the ionization and charge exchange reactions.

$$\dot{n}_{cap} = (R_{cx} + R_{iz}) n_{sn} n_{e,r} \left(\frac{\Psi}{\Psi_r}\right)^{\alpha} \tag{3.11}$$

To find the total capture rate, the reaction rate equations are summed over the control volume through integration, using Ψ^* as the boundary condition. With $\dot{N}_{cap} = \int \dot{n}_{cap} dV$ the total capture rate becomes:

$$\dot{N}_{cap} = \int (R_{cx} + R_{iz}) n_{sn} n_{e,r} \left(\frac{\Psi}{\Psi_r}\right)^{\alpha} dV \tag{3.12}$$

Each neutral captured from the stream by the dipole brings with it a unit of kinetic energy so that the resulting power captured from the stream is:

$$P_{cap} = \frac{m_{sn} u_\infty^2}{2} \dot{N}_{cap} \tag{3.13}$$

3.2.3 Power Balance

The power balance within the dipole can be simply written as:

$$P_{in} = P_{out} \tag{3.14}$$

P_{in} is defined as the sum of the power captured P_{cap} and the power from the initial plasma injected P_{inj} into the dipole.

$$P_{in} = P_{cap} + P_{inj} \tag{3.15}$$

P_{out} is approximated using the N_{tot} to represent the total population of ions and electrons exiting the control volume at an average rate of τ_{tot}. Approximating the power lost in this way allows for an exploration of the general scaling and physics. A detailed accounting of exactly how the power is being lost is left to future work.

$$P_{out} = \frac{N_{tot}}{\tau_{tot}} \tag{3.16}$$

3.3 Plasma Aerocapture with Dissociation

The inclusion of dissociation into the plasma aerocapture model necessitates accounting for H in addition to H2 in the interaction between the neutral stream and the plasma dipole because H2 creates H within the stream prior to reaching the control volume. The process for finding the representative equations for the interaction between the neutral stream and the plasma dipole is similar to the case without dissociation. The geometry remains the same so that only the change in density along z is considered, and the same scaling for the electron density is applied. Subscripts in the following equations are supplemented with either an H or $H2$ to differentiate between the species. This gives the coupled equation set:

$$\frac{\partial n_{sn,H2}}{\partial z} = -R_{diss} n_{sn,H2} n_{e,r} \left(\frac{\Psi}{\Psi_r}\right)^{\alpha} - R_{iz,H2} n_{sn,H2} n_{e,r} \left(\frac{\Psi}{\Psi_r}\right)^{\alpha} - R_{cx,H2} n_{sn,H2} n_{H2+} \tag{3.17}$$

$$\frac{\partial n_{sn,H}}{\partial z} = +2R_{diss} n_{sn,H2} n_{e,r} \left(\frac{\Psi}{\Psi_r}\right)^{\alpha} - R_{iz,H} n_{sn,H} n_{e,r} \left(\frac{\Psi}{\Psi_r}\right)^{\alpha} - R_{cx,H} n_{sn,H2} n_{H+} \tag{3.18}$$

In this case, because of the increased number of species, the charge neutrality assumption ($n_e = n_{H+} + n_{H2+}$) does not help simplify the equations. To solve the equations, a new parameter κ is introduced, which represents the ratio of ion densities considered. The definition of κ in combination with the charge neutrality assumption is used to simplify the continuity equations so that they can be solved.

$$\kappa = \frac{n_{H+}}{n_{H2+}} \tag{3.19}$$

$$n_{H2+} = n_e \left(\frac{1}{1+\kappa}\right) = n_{e,r} \left(\frac{\Psi}{\Psi_r}\right)^{\alpha} \left(\frac{1}{1+\kappa}\right) \tag{3.20}$$

$$n_{H+} = n_e \left(\frac{\kappa}{1+\kappa} \right) = n_{e,r} \left(\frac{\Psi}{\Psi_r} \right)^{\alpha} \left(\frac{\kappa}{1+\kappa} \right) \tag{3.21}$$

Substituting the definitions for the ion densities in terms of κ into the continuity equations results in their final form:

$$\frac{\partial n_{sn,H2}}{\partial z} = \frac{n_{e,r}}{u_\infty} \left(\frac{\Psi}{\Psi_r} \right)^{\alpha} n_{sh,H2} \left(-R_{diss} - R_{iz,H2} - R_{cx,H2} \left(\frac{1}{1+\kappa} \right) \right) \tag{3.22}$$

$$\frac{\partial n_{sn,H}}{\partial z} = \frac{n_{e,r}}{u_\infty} \left(\frac{\Psi}{\Psi_r} \right)^{\alpha} \left(2R_{diss} n_{sn,H2} - R_{iz,H} n_{sn,H} - R_{cx,H} n_{sn,H} \left(\frac{\kappa}{1+\kappa} \right) \right) \tag{3.23}$$

Physically, these equations show that for the steady state case, the dissociation, ionization, and charge exchange reactions decrease the neutral H2 population. Dissociation adds to the H population while ionization and charge exchange subtract from it. Note that for both H2 and H, only resonant charge exchange is considered.

3.3.1 Power Captured

Power captured is found in the same way as the non-dissociation case but with the inclusion of H. First, the capture rate of the particles is defined again following [14]:

$$\dot{N}_{cap,H2} = \int (R_{cx,H2} + R_{iz,H2}) n_{sn,H2} n_{e,r} \left(\frac{\Psi}{\Psi_r} \right)^{\alpha} dV \tag{3.24}$$

$$\dot{N}_{cap,H} = \int (R_{cx,H} + R_{iz,H}) n_{sn,H} n_{e,r} \left(\frac{\Psi}{\Psi_r} \right)^{\alpha} dV \tag{3.25}$$

$$\dot{N}_{cap,Tot} = \dot{N}_{cap,H2} + \dot{N}_{cap,H} \tag{3.26}$$

Using the definition of $\dot{N}_{cap,Tot}$ the total power captured from the steam is given as:

$$P_{cap,Tot} = \frac{(m_{sn,H2} + m_{ns,H}) u_\infty^2}{2} \dot{N}_{cap,Tot} \tag{3.27}$$

3.3.2 Power Balance

The form of the power balance remains the same as in the non-dissociation case. Substituting the relevant terms gives:

$$P_{in} = P_{cap,Tot} + P_{inj} \tag{3.28}$$

$$P_{out} = \frac{N_{tot}}{\tau_{tot}} \tag{3.29}$$

In this case, the terms in P_{out} represent additional species compared to the case without dissociation.

Chapter 4

MODEL IMPLEMENTATION

In this chapter, the method of implementation in Mathematica is described first. Then, the specific spacecraft parameters used in the analysis are defined and explained. Finally, the cross-sections and reaction rates used are presented.

4.1 Method

Both models were implemented in Mathematica. The case without dissociation was less computationally intensive and is described first. Since the general setup for both models is identical, commonalities between the two cases are highlighted in the description of the model without dissociation. With dissociation, the increase in the number of variables used necessitated iterative methods to find a solution. This increased the complexity and computational load for finding a solution. Methods used to find a solution for the case with dissociation are described last.

In both cases, the relevant cross-sections and reaction rates were defined first. Simplifying assumptions and sources used for these are described in greater detail in the following section. Generally, in the cases where the reaction rate was defined as the interaction between a beam and stationary particle, a representative cross-section was chosen. In some cases, it was more appropriate or necessary to model the reaction rate as an interaction between a stationary particle and a Maxwellian. For these cases, a table was created for the appropriate temperature range and then interpolated. The refinement of the table for a given set was balanced against the computational load and how accurate the resulting fit was. Step sizes for temperature ranged between 0.01 eV and 0.001 eV.

Once the reaction rate was defined, the spacecraft parameters ($u\infty$, $n\infty$, B_0, r_c,P_{inj})

were determined, and the desired range for the n_{er} and T was defined. Next, the functions for Ψ, I_{snH2}, and I_{snH} were inputted. Equations for these functions can be found in the preceding chapter.

Finally, the differential equations for the neutral densities were solved using the built-in function ParametricNDSolve. This function is an LSODA solver. Mathematica finds the solution through an iterative process by testing different step sizes and methods until a valid solution is found for a defined accuracy and precision [28]. The solution output is in the form of an interpolating function.

The resulting solution gives the number density of the flow for the defined spacecraft parameters at a specified location as an interpolating function. The interpolating function is inputted to the I_{sn} function for a defined ρ_L value. The solution to this is used to find N_{cap} and then P_{cap}. The ParametricNDSolve function is wrapped in the Table function, to automate the process of finding multiple solutions at different conditions of n_{er} and T. The output generated is a Table containing the following values per solution set: n_{er}, T, N_{cap}, and P_{cap}.

For the case with dissociation, the general process described above remained the same, however, there is an additional step into which the ParametricNDSolve is nested since the value of κ must be found implicitly. After the relevant cross-sections, reaction rates, and spacecraft parameters were determined, an initial guess for the value of κ was chosen. This value was taken to be $\kappa = 1$ for all cases. Unity for κ physically represents equality between densities for H2 and H and allowed for reasonably quick convergence in the first iteration. This κ value was fed into the ParametricNDSolve function where solutions for $n_{H2,sn}$ and $n_{H,sn}$ were found. The solutions were then used to calculate the corresponding $N_{cap,H2}$, $N_{cap,H}$, $P_{cap,H2}$, and $P_{cap,H}$ values as previously described. Using these results, the ratio of $\frac{N_{cap,H}}{N_{cap,H2}}$ was calculated as an approximation of κ. If the calculated value was within 1% of the initial value, the initial value was saved as the final κ value. If the calculated value was not within 1% of the initial value, the calculated value was defined as the new initial value. The loop continued to iterate until the calculated value converged to be within 1% of the initial value. Then, the Table function moved on to the next set of n_{er} or T being investigated.

The output generated for the case with dissociation was: n_{er}, T, $N_{cap,H2}$, $N_{cap,H}$, $P_{cap,H2}$, $P_{cap,H}$, and κ. A running log of the κ value generated during each loop was kept in a separate table to track convergence. Solutions for κ converged on average in just under a minute. For some temperatures and spacecraft conditions, it was found that the κ values would go negative and have trouble converging. Since the regimes in which this was happening were clearly non-physical, if this occurred, the computation was halted, and the maximum density reduced to the next previous value which had converged. In this way, negative oscillations were prevented and the solutions could be relied upon to represent physical processes. An example of the convergence for κ alongside the resulting density values is shown below in Figures 4.2 and 5.3. The exponential increase in the κ value is occurring at the point where the density of H2 is dropping sharply. Given the definition of κ, this makes sense; its denominator is becoming very small resulting in a large value.

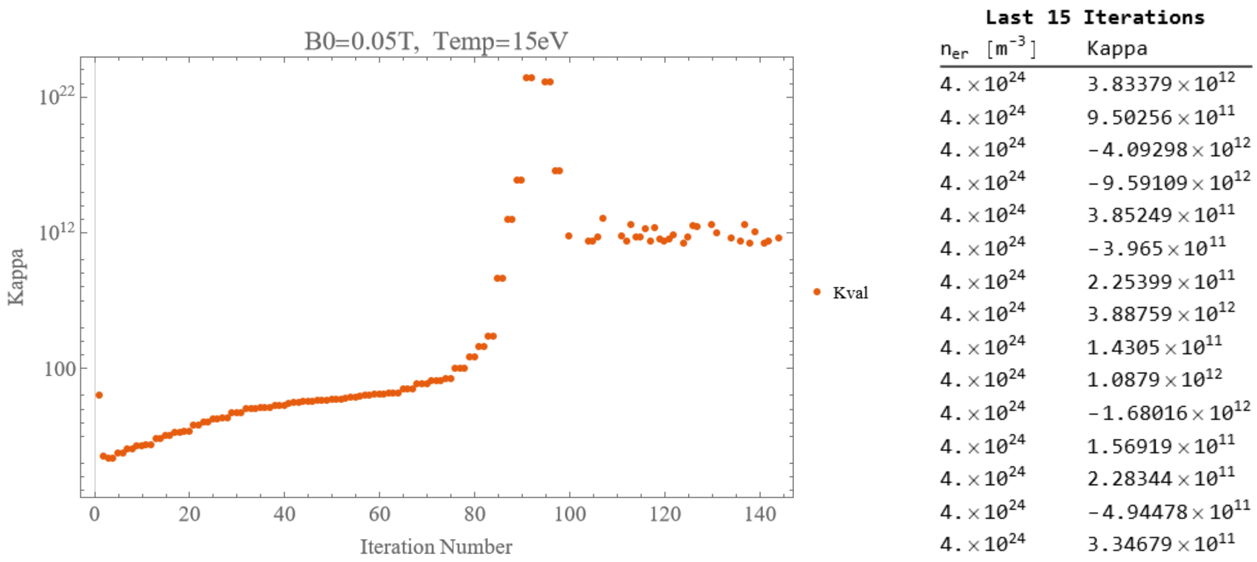

Last 15 Iterations

n_{er} [m^{-3}]	Kappa
$4.\times10^{24}$	3.83379×10^{12}
$4.\times10^{24}$	9.50256×10^{11}
$4.\times10^{24}$	-4.09298×10^{12}
$4.\times10^{24}$	-9.59109×10^{12}
$4.\times10^{24}$	3.85249×10^{11}
$4.\times10^{24}$	-3.965×10^{11}
$4.\times10^{24}$	2.25399×10^{11}
$4.\times10^{24}$	3.88759×10^{12}
$4.\times10^{24}$	1.4305×10^{11}
$4.\times10^{24}$	1.0879×10^{12}
$4.\times10^{24}$	-1.68016×10^{12}
$4.\times10^{24}$	1.56919×10^{11}
$4.\times10^{24}$	2.28344×10^{11}
$4.\times10^{24}$	-4.94478×10^{11}
$4.\times10^{24}$	3.34679×10^{11}

(a) (b)

Figure 4.1: This plot displays the convergence of κ over time as the program looped through different densities at a fixed temperature and magnetic field strength. The Table shows the density value at the final 15 iterations and the corresponding κ.

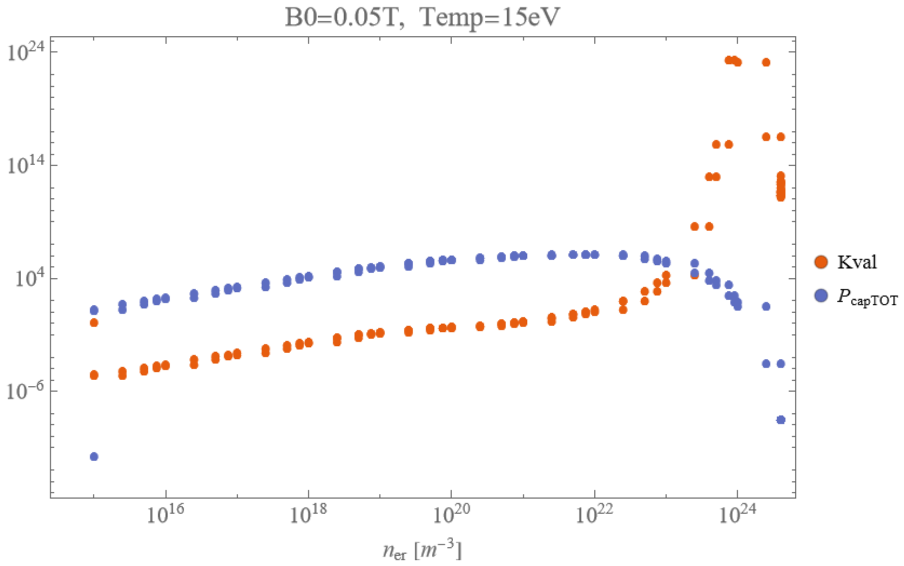

Figure 4.2: The plot displays the final converged value of κ for a given density at the specified conditions alongside the corresponding total power captured $P_{cap,Tot}[J/s]$.

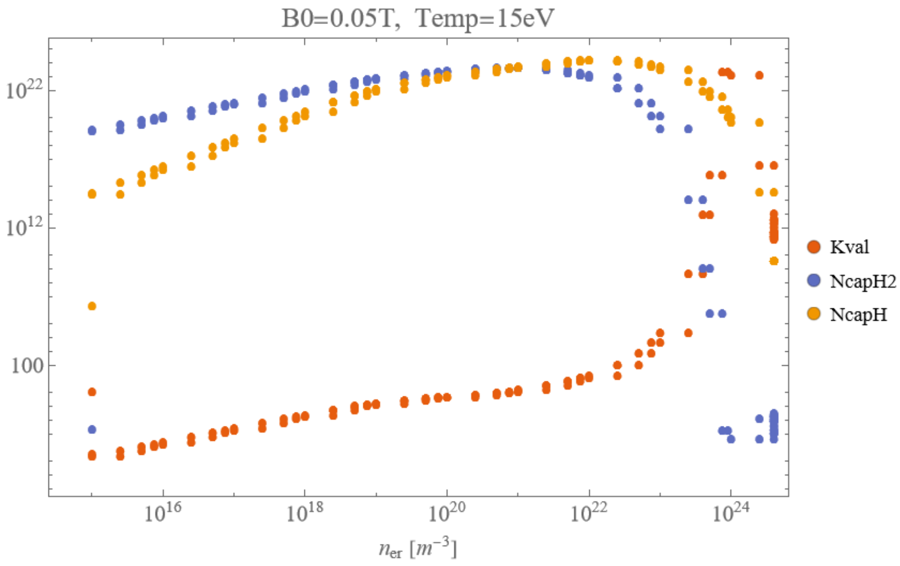

Figure 4.3: The plot displays the final converged value of κ for a given density at the specified conditions alongside the corresponding captured densities of H2, $N_{cap,H2}[m^{-}3]$, and H, $N_{cap,H}[m^{-}3]$.

The processes described above required inputs in ranges physically representative and useful to the study of plasma aerocapture. In the following sections, the spacecraft and model parameters, specific cross-sections, and reaction rates, which were used as inputs to the model are outlined.

4.2 Spacecraft and Neutral Stream Parameters

The spacecraft parameters for this system are the center magnetic field strength, B_0, the magnet radius r_c, and the velocity of the stream neutrals at infinity, u_∞. The Neutral Stream parameters are the species and the density of the stream neutrals at infinity, n_∞.

4.2.1 Species

H2 is chosen as the species for this model because the atmospheres of many destinations where MAC is an enabling technology (Neptune, Uranus, Saturn) are largely composed of Hydrogen. The cross-sections and reaction rates for H2 are also readily available in the literature.

4.2.2 Magnet center field strength

In the model, magnet strength is varied between 0.01 T and 1 T. The range encapsulates magnet strengths used by others in their models. Previous studies have shown that this range of field strength is achievable with currently available technology without taking on huge increases in mass for a PPU [13] [2] [12] [3]. The value of B_0 impacts ρ_L, and subsequently the size of the control volume. Larger values of B_0 lead to a greater capture area.

4.2.3 Magnet Radius

The magnet radius is taken to as $r_c = 1$, following the MAC design laid out in [13]. It is similar in magnitude to the magnet design choices made by others [2] [12] [3]. This value

Destination	Approach Velocity [m/s]	ΔV [m/s]	Velocity Range [m/s]
Saturn	35,000	8,000	27,000 to 35,000
Neptune	29,000	6,000	23,000 to 29,000
Uranus	24,000	4,500	19,000 to 24,000
Venus	11,700	4,600	7,100 to 11,700
Mars	5,900	1,200	4,700 to 5,900

Table 4.1: Approach velocities and ΔV values for relevant destinations.

is not varied in the implementation of the model, but given that it also appears in the denominator of ρ_L, its impact should be similar to that of the magnetic field strength.

4.2.4 Stream velocity

The neutral stream neutral velocity is representative of the spacecraft's approach velocity at its destination. In the cases where the reaction rate is modeled as the interaction between a beam and a stationary molecule, the stream velocity is analogous to the beam velocity, such that $u_\infty = v_b$.

Values for the neutral stream velocity were chosen based on the relevant approach velocities for Neptune because MAC provides the most benefit at the Ice Giants where it is a mission-enabling technology. [29] and [9] both list $29000 m/s$ as a possible approach velocity for Neptune. [9] additionally gives the approach velocities and δV for a variety of locations, which are adapted in a table below:

As seen in Table 4.1, choosing $29000 m/s$ allows for the results to be directly applied to a variety of cases. To inspect the impact of velocity on the resulting power captured, a value of $23000 m/s$ was run as well. This value represents the lower end of spacecraft velocity at Neptune and intersects with the velocity range at Uranus.

4.2.5 Stream Density

The stream density is taken to be either 10^{18} or 10^{19}. This value was chosen because it represents a good median density for altitudes relevant to MAC at Saturn, Neptune, and Uranus. Specifically, according to [13], these densities correspond to altitudes between 400 and 700 km for Neptune and 650 to 800 km for Saturn. Examining two different densities allowed for general observation of how an increase in density might be influenced by the inclusion of dissociation. An accounting of mass and energy within the control volume would be needed to fully determine its impact.

4.3 Cross Sections and Reaction Rates

Electron impact ionization of H2 and charge exchange of H2 are considered in both the case without dissociation and the case with dissociation. For the case with dissociation, electron impact ionization of H, charge exchange of H, and dissociation of H2 are additionally considered.

4.3.1 [$H + e^- \rightarrow H^+ + 2e^-$] H Electron Impact Ionization

Janev et al. [30] give an analytical expression for the electron impact ionization cross-section for the ground (1s) and metastable excited states (2l, 3l) as reproduced below. E is the collision energy in eV, $I_n = 13.6/n^2$ is the ionization potential corresponding to the level, n. The fit is zero at $E = 13.6$. The expression is applied for $n = 1$ within the model, so that only the case from the ground state is considered. In the region the accuracy of the fit is stated as being within 10% of the data used to create the fit.

$$\sigma_{izH} = \frac{10^{-13}}{I_n E}[A_0 ln(E/I_n) + \sum_{j=1}^{5} A_j(1 - \frac{I_n}{E})^j] * 10^{-4}[m^2] \tag{4.1}$$

n = 1 $\quad I_n = 13.6/n^2 \quad A_0 = 0.18450 \quad A_1 =$ -0.032226

$A_2 =$ -0.034539 $\quad A_3 = 1.4003 \quad A_4 =$ -2.8115 $\quad A_5 = 2.2986$

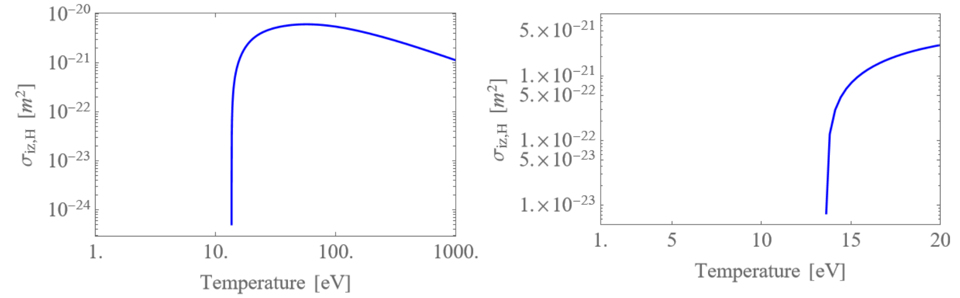

Figure 4.4: Cross section for the electron impact ionization of H. On the right, is a larger range, and on the left is the range that was used in the model[30].

The reaction rate is calculated using the assumptions outlined in [31] for $v1 >> v2$, under the assumption that H is stationary with respect to e. This assumption is reasonable here because the velocity of the electrons should be much greater than the velocity of the much heavier neutrals. The results are interpolated in Mathematica and are displayed below along with the equation.

$$< \sigma v >_{izH} = \int_o^\infty \left(\frac{m_e}{2\pi T_e e}\right)^{3/2} e^{\frac{-m_e v^2}{2T_e e}} 4\pi v^2 \sigma_{izH}\left[\frac{m_e v^2}{2e}\right] v\,dv\ [m^3/s] \tag{4.2}$$

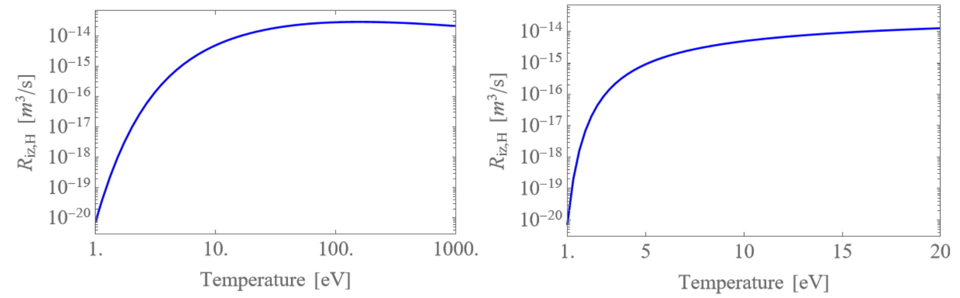

Figure 4.5: Reaction rate for the electron impact ionization of H. On the right is the full range for which the reaction rate was calculated, and on the left is the range that was used in the model.

4.3.2 *[$H + H^+ \rightarrow H^+ + H$] H and H+ Charge Exchange*

The cross-section for a full range of values is given by Barnett et al. [32]. $T_i(X)$ are the Chebyshev orthogonal polynomials. The equation from Barnett et al. and the plot are reproduced below.

$$\sigma_{HHpluscx} = \exp\left[\frac{A_0}{2} + \sum_{i=1}^{k} a_i T_i(X)\right] \tag{4.3}$$

$$X = [(lnE - lnE_{min}) - (lnE_{max} - lnE)]/(lnE_{max} - lnE_{min}) \tag{4.4}$$

a_0=-72.6656 a_1=-5.49142 a_2=-3.42948 a_3=-1.98377

a_4=-0.878809 a_5=-0.198932 a_6=0.0837431 a_7=0.121252

a_8= 0.0827182 $E_{min} = 1.2 * 10^{-1}$ $E_{max} = 6.3 * 10^5$

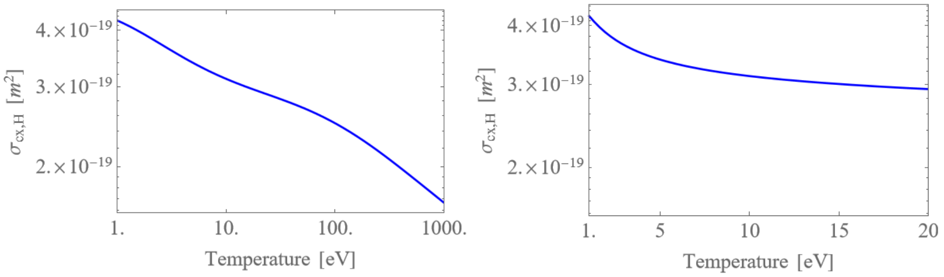

Figure 4.6: Cross section for the electron impact ionization of H. On the right, is a larger range, and on the left is the range that was used in the model[32].

Within the model, a static cross-section is used to simplify the calculations and lighten the computational load. A value of $\sigma_{cxHHplus} = 3.00914 * 10^{-19}[m^2]$ is chosen. This value is reasonable for the temperature range ($2 - 20eV$) used in the model. At lower temperatures, the cross-section is slightly larger but drops off to a more constant value around $T = 7eV$. This implies that the ionization rate will be slightly under-predicted at those temperatures. Using the static cross-section and a beam velocity of 29000[m/s] the resulting $R_{cxHHplus}$ is below.

$$R_{cxHH+}v = 3.00914 * 10^{-19} * 29000 = 8.73 * 10^{-15}[m^3/s] \tag{4.5}$$

4.3.3 [$H2 + e^- \rightarrow H^+ + 2e^-$] H2 Electron Impact Ionization

Janev et al. give the cross-section for the electron impact ionization of H2 [30]. There are three different channels discussed for the ionization from the ground state, here, the non-dissociative ionization channel is used. The fit and plot are reproduced below. Within the expression, E is the temperature is eV, C_0 is a constant, and δE is the threshold energy for the specified ionization channel.

$$\sigma_{ion}^{ndiss}(^2\Sigma_g^+)_0 = \frac{1.828}{x}(1 - \frac{1}{x^{0.92}})^{2.19} ln(C_0 x) * 10^{-20}[m^2] \tag{4.6}$$

$$C_0 = 2.05 * \delta E \quad \Delta E = 15.42[eV] \quad x = E/\Delta E$$

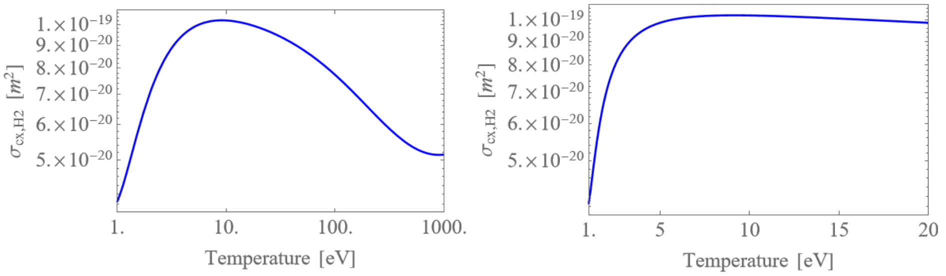

Figure 4.7: Cross section for the electron impact ionization of H2. On the right, is a larger range, and on the left is the range that was used in the model[32].

The reaction rate is again found using [31] and assuming that $v_e >> v_{H2}$ (ie that $H2$ is stationary with respect to e) as in the calculation of the reaction rate for the electron impact ionization of H. A plot with the reaction rate values is shown below.

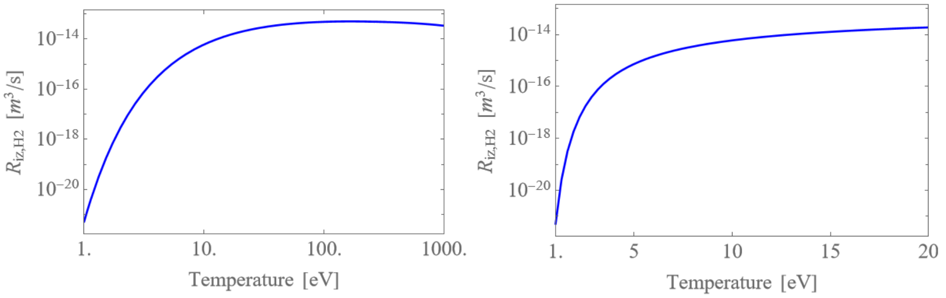

Figure 4.8: Cross section for the electron impact ionization of H. On the right, is a larger range, and on the left is the range that was used in the model[32].

4.3.4 $[H + H^+ \rightarrow H^+ + H]$ H2 and H2+ Charge Exchange

The cross-section for charge exchange between H2 and H2+ is sourced from Janev et al.[30]. The authors note that the data sources from which the fit is created have good agreement above $5eV$. Below $5eV$ there is significantly less data available. The data which does exist varies significantly across studies. The authors note that fluctuations in the cross-section result from competing reactions in certain regions. The temperatures explored in this model overlap with the regions where there are fluctuations. Specifically, results are collected at $1eV$ and $5eV$. The equations and plots reproduced below for the fit are 207a, 207b, and 207c. E here is the energy in eV.

$$\sigma_{HH+cx} = \sigma_{CX}^{<} + \sigma_{CX}^{>}[m^2] \tag{4.7}$$

$$\sigma_{CX}^{<} = \frac{6.59}{E^{0.5}(1+2.29E^{1.78})} + \frac{12.85exp(-1.84/E^{1.55})}{E^{0.0673}(1+2.60*10^{-3}E^{0.97}+1.63*10^{-10}E^{2.76})} * (10^{-20}) \tag{4.8}$$

$$\sigma_{CX}^{>} = \frac{11.38exp(-61.80/E^{0.54})}{1+8.21*10^{-10}E^{2.08}+3.80*10^{-26}*E^{5.15}} * (10^{-20}) \tag{4.9}$$

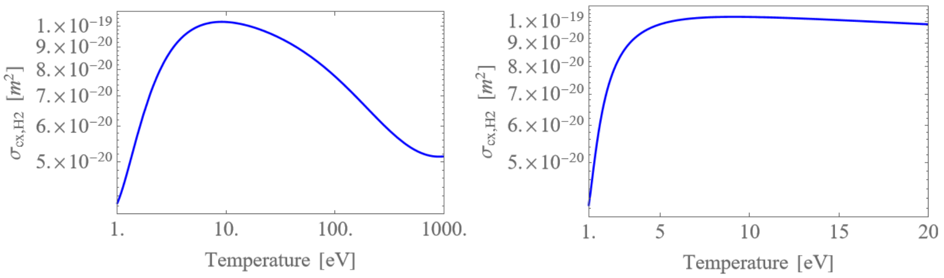

Figure 4.9: Cross section for charge exchange between H2 and H2+. On the right, is a larger range, and on the left is the range that was used in the model[32].

As with the reaction rate for charge exchange between H and H+, a static cross-section is chosen here to reduce computational load and simplify the calculation. A value of $\sigma_{cxH2H2+} = 1.00613*10^{-19}$ is used based on observation of the cross-sectional trends. Between 1 and 5 eV, the cross-section increases quickly, before leveling off around 7 eV for the region of interest. The σ value chosen means that the resulting reaction rate will be slightly over-predicted at lower temperatures.

$$R_{cxH2H2+} = 1.00613 * 10^{-19} * 29000 = 2.92 * 10^{-15} [m^3/s] \tag{4.10}$$

4.3.5 $[H2 + e^- \rightarrow H + H + e^-]$ H2 Electron Impact Dissociation

The cross-section for the electron impact dissociation was first found experimentally by Corrigan et al.[33] for energies between 8.8 and 95 eV. They predicted that the measured cross-section was being overestimated due to the possibility of the molecular ionization cross-section being included in their measurements. Since that experimental result, there have been additional theoretical models[34], but no experimental ones [35]. Using the available data, Yoon et al. recommend cross-sectional values for a range of temperatures between 9 and 80 eV. A fit is created by interpolating between those data points and is shown below.

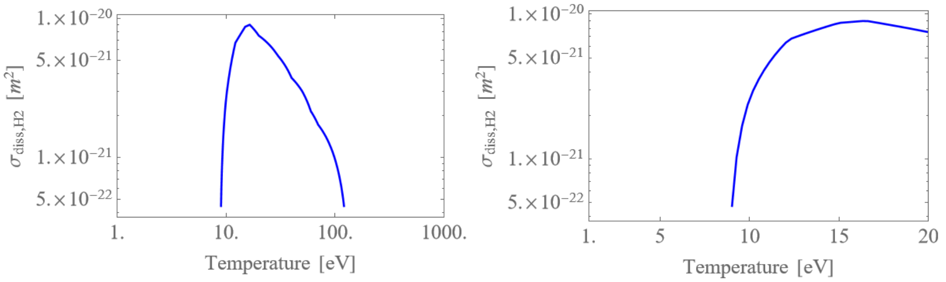

Figure 4.10: Cross section for the electron impact dissociation of H2. On the right is a larger range, and on the left is the range that was used in the model[35].

The reaction rate is again found using [31] and assuming that $v_e >> v_{H2}$ (i.e. that $H2$ is stationary with respect to e) as in the calculation of the reaction rate for the electron impact ionization of H and H2. A plot with the reaction rate values is shown below. In these plots, the expression for the reaction rate provided by Janev et al. is also shown. The value for the calculated reaction rate is several orders of magnitude larger than what they found.

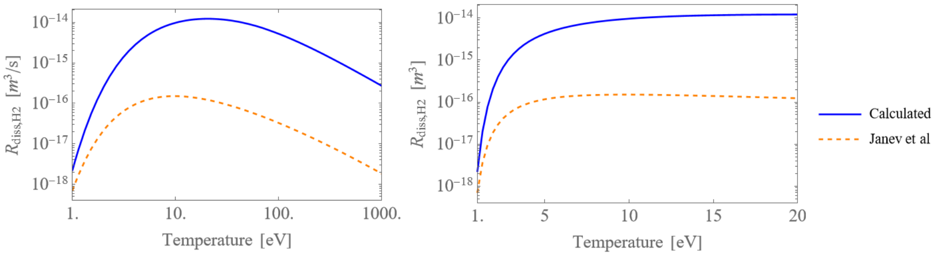

Figure 4.11: Reaction rate for the electron impact dissociation of H2. On the right, is a larger range, and on the left is the range that was used in the model[30].

4.3.6 All Cross Sections and Reaction Rates

All cross-sections used in the model are presented below. The charge exchange cross sections are static and are several orders of magnitude larger than the others at all temperatures. Dissociation and ionization dominate in different temperature ranges. Below about $75eV$, dissociation dominates above ionization. For the range of interest, between $1eV$ and $20eV$, the dissociation cross section is larger than the ionization cross sections.

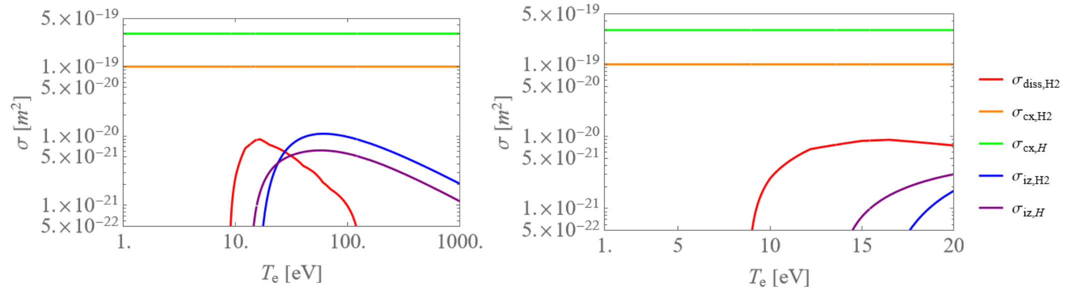

Figure 4.12: All included cross sections. On the right, is a larger range, and on the left is the range that was used in the model[30].

All reaction rates used in the model are presented below. From 1 to 5 eV, the reaction rates for the charge exchange are several orders of magnitude larger than the other reaction rates. Dissociation and ionization for both species increase exponentially from 1 to 10 eV and then level out at a magnitude about equal to the charge exchange cross section for H

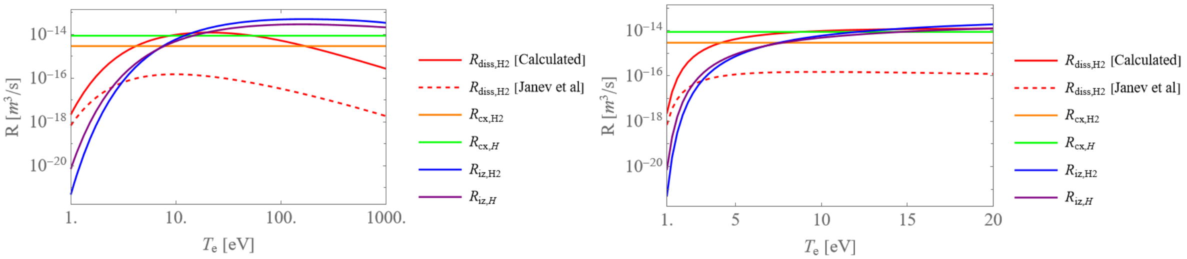

Figure 4.13: All included reaction rates. On the right, is a larger range, and on the left is the range that was used in the model[30].

Chapter 5

RESULTS

Using the expressions developed in Chapter 3, alongside the spacecraft and model parameters, and the reaction rates and cross sections detailed in Chapter 4, a control volume analysis is completed for the interaction between a neutral beam and plasma dipole. Results for the case without dissociation are presented first, then the case with dissociation. Finally results from the two studies are compared to find the impact of including dissociation in the model. Nominal conditions for the model are $u_\infty = 29000 m/s$, $n_\infty = 10^{18} m^{-3}$, and $r_c = 1m$. These values are used unless otherwise indicated. Subsections indicate which parameters are varied. For the case without dissociation, only the magnetic field and temperature are varied because trends related to other parameters can easily be extrapolated to the simpler case. With dissociation, n_∞ and u_∞ are additionally varied.

5.1 Plasma Aerocapture without Dissociation

5.1.1 Varying Magnetic Field and Temperature

Figures 5.1 and 5.2 display the results for the case without dissociation. Each subplot represents a fixed magnetic field strength or temperature, respectively while varying the other parameter. In both cases, the temperature considered are $2, 5, 10, 15, and 20 eV$. Magnetic field strengths considered are $1, 0.5, 0.25, 0.05, and 0.01T$. Consistent trends can be observed with both the increasing temperature and magnetic field strength.

In Figure 5.1, the influence of temperature at a set magnetic field strength can be observed. This impact is minimal, but present, for every magnetic field strength. The width of the parabola representing the power captured by the plasma dipole at a given magnetic field strength is consistent as the temperature increases. The density range over which the parabola exists begins and ends at a lower plasma density for higher temperatures compared to lower temperatures. This happens because, at higher temperatures, more energy can be deposited into the plasma. Specifically, increasing the temperature changes the magnitude of the reaction rates and their relative ratios to each other. Here, electron impact dissociation and charge exchange of H2 are the reaction rates considered. The reaction rate for charge exchange is taken to be a constant value, regardless of temperature, so the shifts in range across temperature are more likely due to the electron impact ionization of H2. At temperatures below $5eV$ the electron impact ionization reaction rate is orders of magnitude smaller than that of charge exchange. Therefore, more of the power captured from the neutral stream by the plasma dipole is due to charge exchange. As the temperature increases, the reaction rate for electron impact ionization increases as well. Around $7eV$, the magnitudes of the two reaction rates are equivalent and the power contribution from both reaction rates is significant. The increase in the ionization reaction rate with temperature means that an equivalent amount of power can be captured at a slightly lower plasma density because the electrons have higher energy.

Comparing across subplots, it is apparent that increases in magnetic field strength result in a higher amount of power captured over a wider range of plasma densities. Changes in temperature have a smaller impact on power captured than magnetic field strength because it does not directly change the effective area of the control volume. The effect of the magnetic field strength is more readily seen in Figure 5.2, where results are plotted for a range of magnetic field strengths at a given temperature. The trends across the different subplots are consistent. The weaker dependence on temperature is apparent here, as in Figure 5.1 with how similar each of the plots in this set appears to each other. For each temperature, the plasma density at which power begins to be captured is nearly identical for every magnetic field strength. This value is lower by about half an order of magnitude between the lowest and highest temperatures. With increasing field strength, the plasma density at which power capture is captured widens by orders of magnitude. For example, the capture width is about one and a half orders of magnitude larger for $B_0 = 0.025$ than for $B_0 = 0.05$. The maximum amount of power that can be captured becomes larger as the magnetic field strength increases.

The impact of the field strength on the power captured is a function of its relationship to ρ_L. As the field strength increases, ρ_L decreases, which corresponds to an increase in the Ψ^* boundary of the control volume and capture region. A greater capture region means more mass and power can be absorbed from the stream. These trends follow the findings of Little et al. [14].

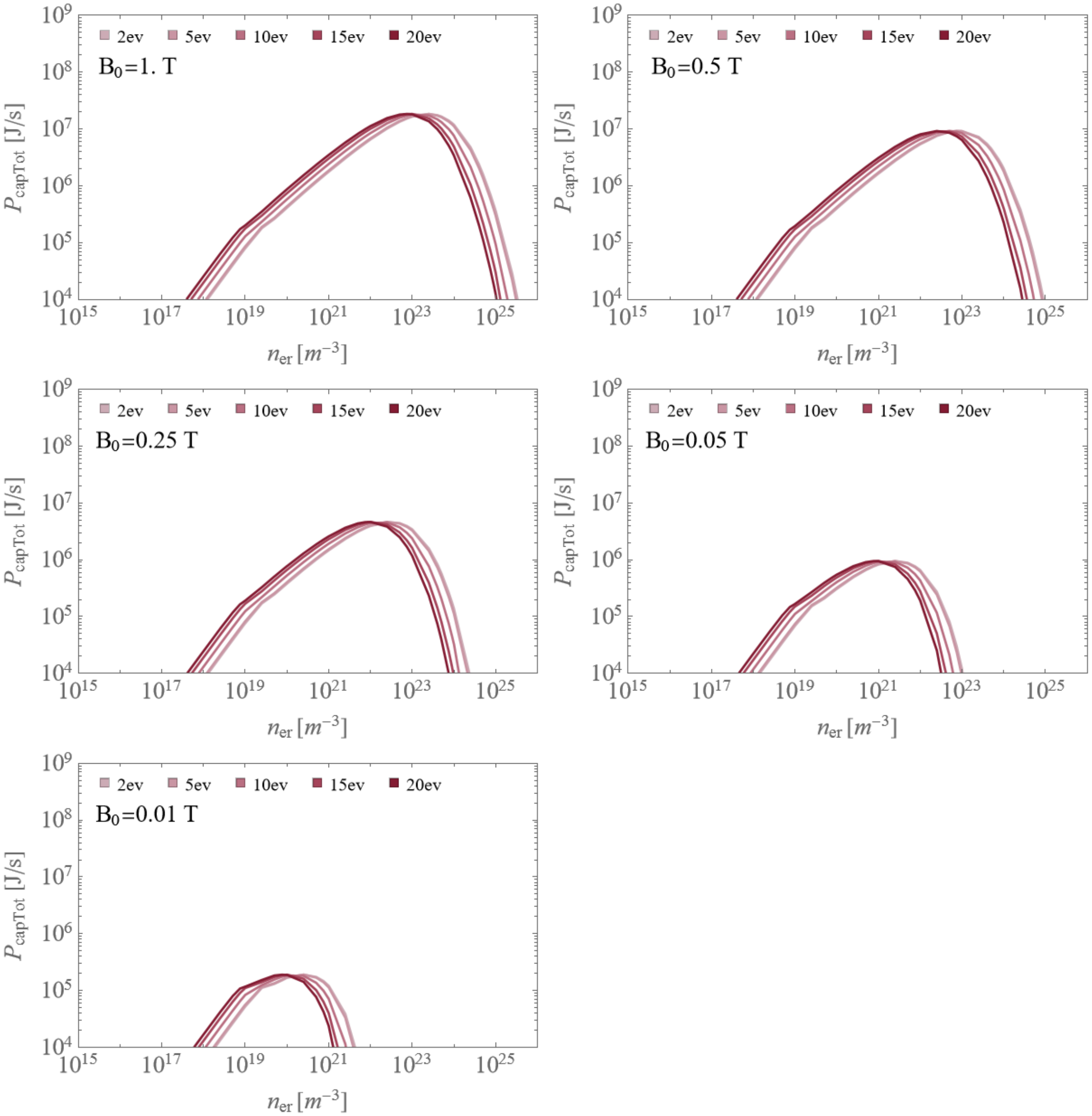

Figure 5.1: Power captured from the neutral stream by the plasma dipole for different temperatures by magnetic field strength.

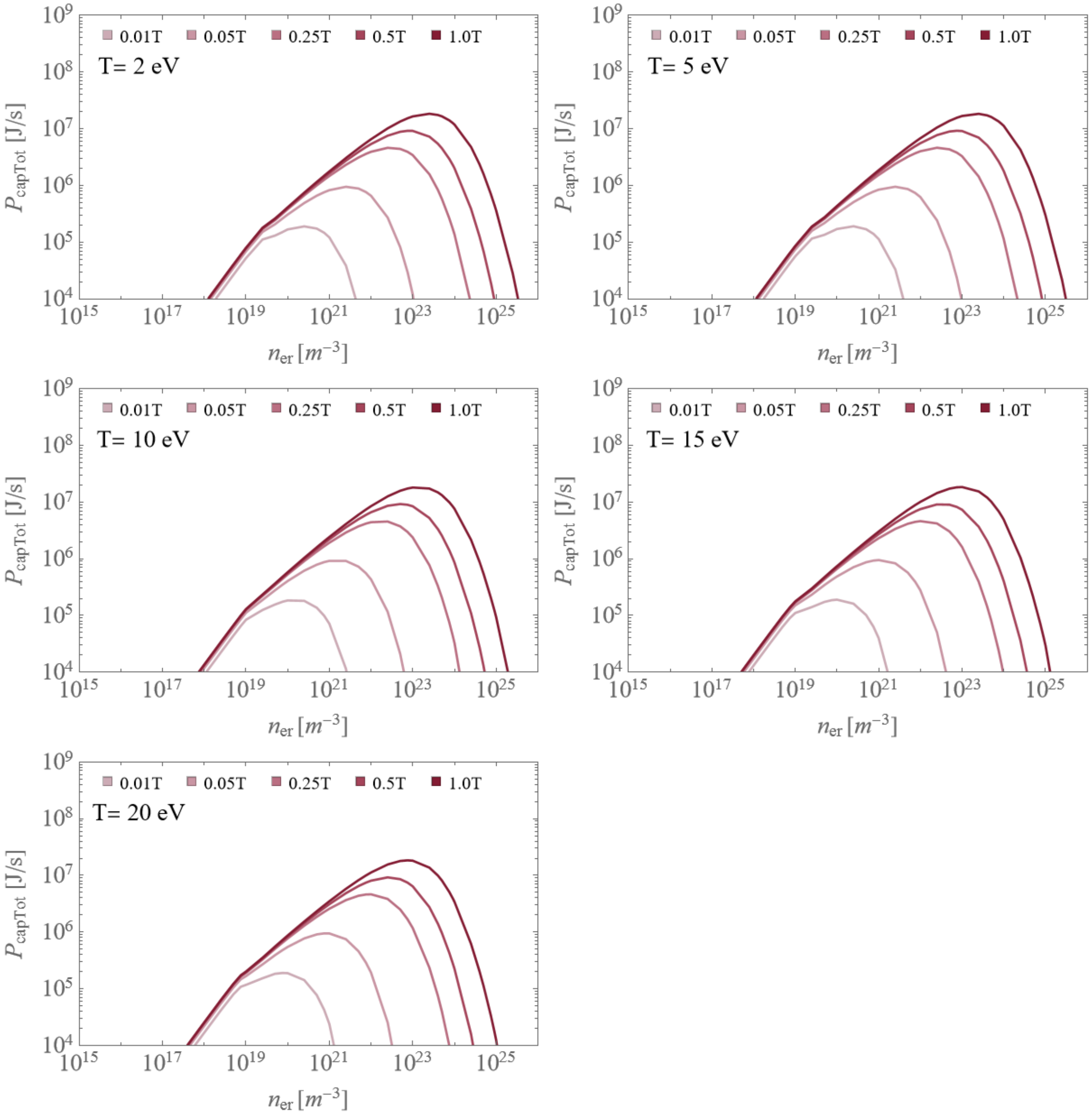

Figure 5.2: Power captured from the neutral stream by the plasma dipole for different magnetic field strengths by temperature.

5.2 Plasma Aerocapture with Dissociation

5.2.1 Kappa Values

Prior to diving into the results for the case without dissociation, the κ values utilized in the calculation of these results are examined. κ represents the ratio of ion densities, $\frac{n_{H+}}{n_{H2+}}$. Large κ values can occur either for very high densities of $H+$ compared to $H2+$ or as a result of very small densities of $H2+$ as compared to $H+$. Small κ values occur in the inverse situations. Figure **??** displays the κ values used for a range of plasma densities and temperatures. Each subplot represents a different magnetic field strength. In both cases, there is a wide range of κ values which increase with both temperature and plasma density. For low temperatures and plasma densities, the κ values are very small, indicating a high $H2+$ density as compared to $H+$. An initial dissociation of $H2$ is needed from the stream in order for the $H+$ ion population to increase, so it makes sense for lower temperatures, where there is a smaller population of H to correspond to regions of lower $H+$. At high densities, across most temperatures, the κ values are very large. As indicated in the methods section, there was a region corresponding to an exponential increase in the κ values corresponding to a drop in the $H2$ population and an increase in the H population. This is visually represented in the contour plots here. For a smaller magnetic field strength, the region of very big κ values is visibly larger and occurs at lower plasma densities, reflecting what has been seen previously in the values of power captured, whereas for stronger magnetic field strengths, capture can occur over a greater area.

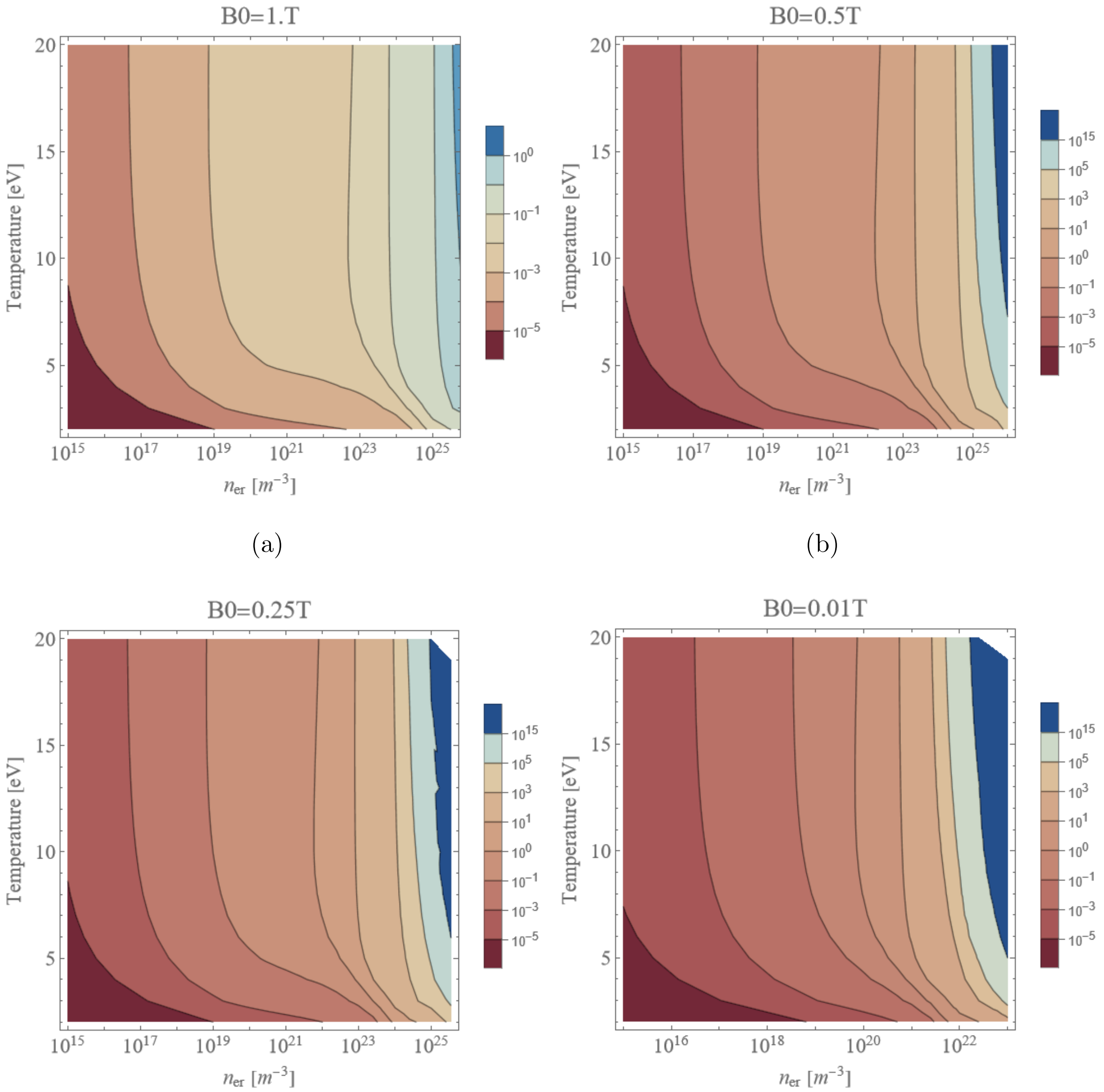

(a) (b)

(c) (d)

Figure 5.3: These plots show the distribution of κ values across a range of plasma densities and temperatures at a given magnetic field strength. The range of temperature is equivalent in each case, but the density range varies.

5.2.2 Varying Magnetic Field and Temperature

Figures 5.4 and 5.5 display the equivalent results to Figures 5.1 and 5.2 for power captured but with dissociation included. Each subplot again represents either a specific magnetic field strength with results plotted for a range of temperatures, or the inverse. The ranges used are equivalent to the case without dissociation. Both series of plots show similar trends as the same series of plots without dissociation.

In Figure 5.4, the temperature is varied for a fixed magnetic field strength. As in Figure 5.1, for a given magnetic field strength, higher temperatures generally do not make a large difference in the range or magnitude of the power captured. In contrast to the results found in Figure 5.1, there is a second peak visible at lower temperature ranges which expands the width of plasma densities where capture can occur. This phenomenon is due to H and displays a clear impact of dissociation.

Like Figure 5.2, Figure 5.5 presents results at fixed temperatures for a range of magnetic field strengths. Similarly to the case without dissociation, the impact of magnetic field strength is more apparent in this configuration. As before, for each temperature, all the magnetic fields are able to begin capture at almost the same density. This shows that for a given temperature, there exists a minimum plasma density where capture becomes viable for a desired level of power captured. The density at which this occurs increases linearly with power. Also similar to Figure 5.2, increasing the magnetic field strength represents an increase in both the range of operating densities as well as the maximum power capture possible. In a deviation from Figure 5.2, and as seen less clearly in Figure **??**, at the lower temperatures, there is a second peak that is visible, indicating that when dissociation is included, a wider range of power capture is visible. The prominence of the second peak decreases with increasing temperature. Its formation is due to H and will be discussed in greater detail in the following section.

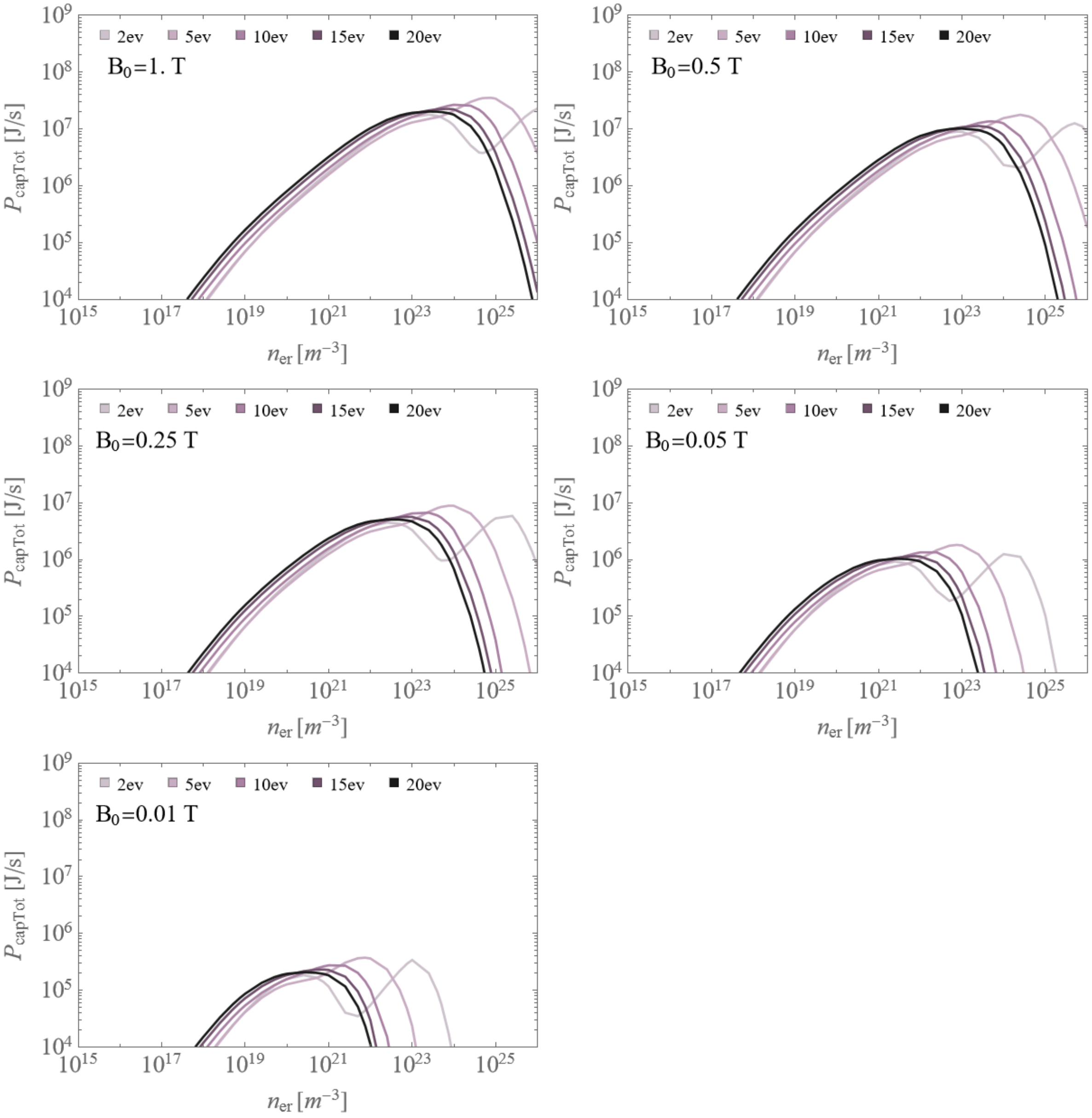

Figure 5.4: Power captured from the neutral stream by the plasma dipole for different magnetic fields by temperature.

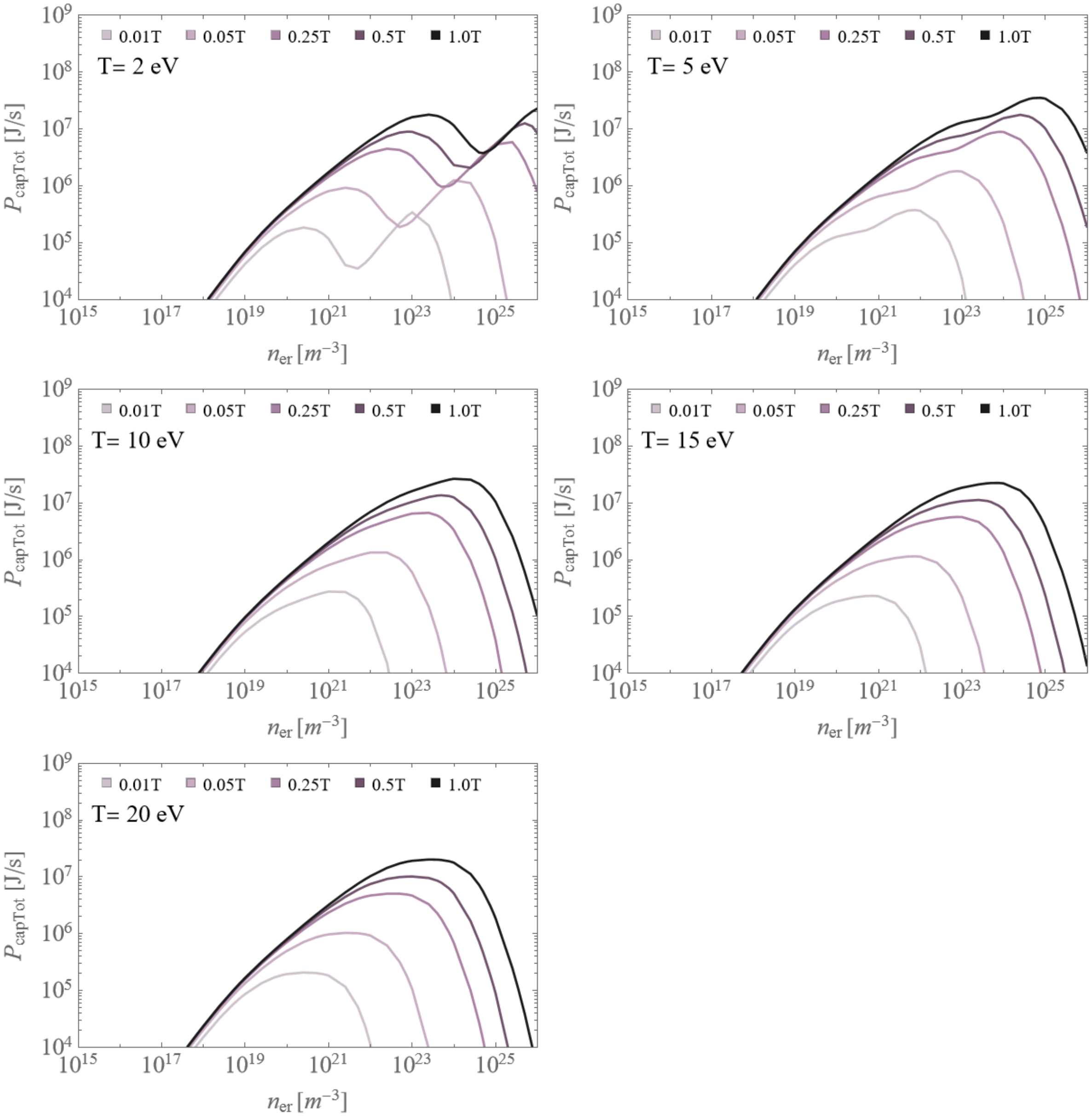

Figure 5.5: Power captured from the neutral stream by the plasma dipole for different temperatures by magnetic field strength.

5.2.3 Varying Stream Density and Velocity

In the following two plots, the neutral stream density and velocity are varied. Within the model, the stream density value is representative of the planetary atmosphere where capture occurs. It comes in as the boundary condition for the stream density at infinity. Increasing this value means that there is a larger amount of neutrals available for capture. Neutral stream velocity is representative of the approach velocity of the spacecraft. In the model varying this parameter will increase the charge exchange cross-section for both H2 and H. This in turn increases the rate at which that reaction occurs within the model.

Figure 5.6 displays the results for an increase in the stream neutral density. Increasing the density from the nominal conditions by an order of magnitude results in an increase in the range of operating plasma densities as well as the maximum possible power captured.

Results from varying the stream velocity are displayed in Figure 5.7. Decreasing the stream velocity from the nominal conditions results in a small decrease in the power captured at lower plasma densities. There is no change visible at higher plasma densities.

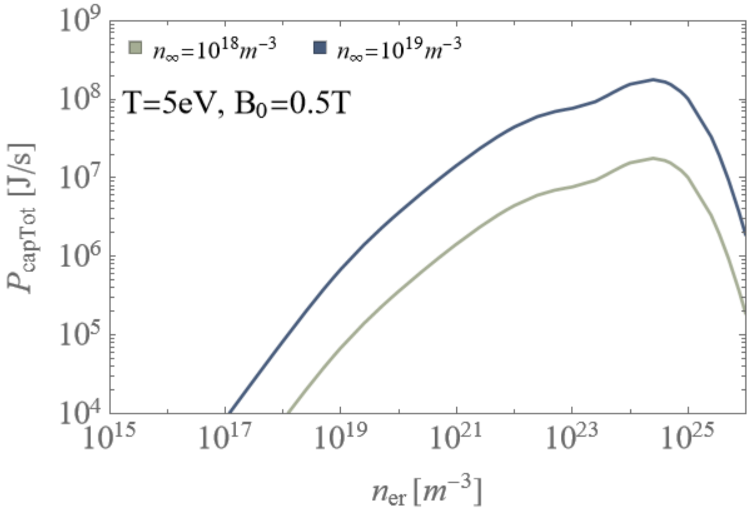

Figure 5.6: Power captured for two different stream neutral densities for $T = 5ev$ and $B_0 = 0.5T$.

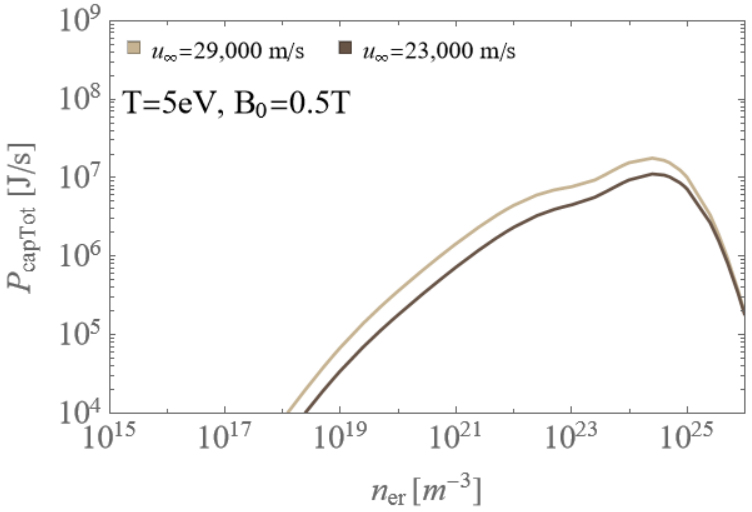

Figure 5.7: Power captured for two different stream velocities for $T = 5ev$ and $B_0 = 0.5T$.

5.3 *Impact of Dissociation*

In assessing the impact of dissociation, it is useful to observe the breakdown in power captured between H and H2. Figure 5.8 provides this comparison. In the right-hand column, Figure 5.5 is reproduced, where power captured at a given temperature is plotted for a range of magnetic field values. In the left-hand column, for a given row, the power captured at the same temperature is plotted by its component parts for a magnetic field strength of $B_0 = 0.25T$. The case without dissociation is also included in this same plot to provide a direct comparison. Trends observed for the lowest temperature will be discussed first. These are then extended to higher temperatures. Finally, changes in the trends with increases in temperature are noted.

For a temperature of $T = 2ev$, the power captured without dissociation follows the same trend as the case with dissociation until slightly past the first peak. At this point, the power captured for the two cases diverges. In the case without dissociation, the power captured drops off, while in the case without dissociation, there is a slight dip in the power captured, after which it increases to a second maximum. The second peak is due to the accounting of H, its location can be attributed to the magnitudes of the reaction rates with respect to each other. At lower temperatures, the reaction rate for the ionization of H is greater than the reaction rate for the ionization of H2. Around 7 eV they are equal, and then the reaction rate for H2 overcomes H slightly. The difference in the magnitudes of the reaction rates for ionization helps to explain why the second peak disappears as the temperature increases. The magnitude of the difference between the reaction rates is greater at lower temperatures, so the differences are more pronounced there. As the temperature increases and the power contribution from reaction rates becomes more equal at the same temperature, the second peak becomes less distinct. Instead, the slope of the curve approaching the maximum power captured becomes flatter. In MAC, power captured from the neutral stream translates to drag. An increase in the maximum possible power capture then translates to a wider operating region for MAC. Overall, power capture occurs over a greater range of plasma densities for the case with dissociation than without.

Across different temperatures, the changes in the range of capture can be attributed to differences in reaction rates. ρ_L is also a contributing factor in how the power captured breaks down between H2 and H. The value for ρ_L will decrease with a decrease in the mass of the species. Since H has a smaller mass than H2, its resulting ρ_L is smaller as well, which corresponds to a larger Ψ^* and a greater capture volume. For all temperatures, the maximum power captured from H is larger than the maximum power captured from H2 because its capture volume is greater. This difference is more pronounced at lower temperatures because of the differences in reaction rates.

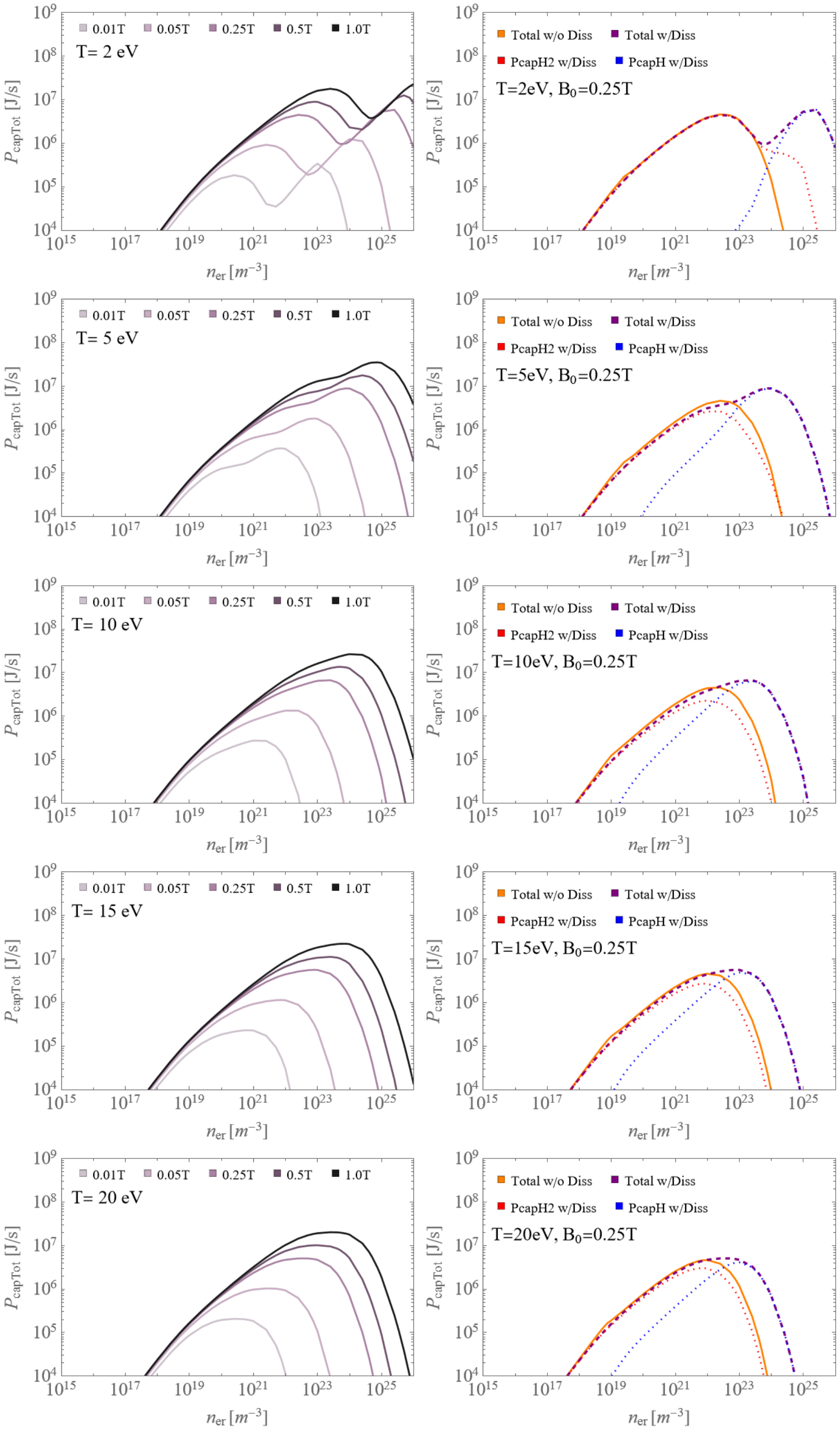

Figure 5.8: The right-hand column replicates Figure 5.4. The left-hand column shows the power breakdown between H and H2 and the total power captured for the corresponding case without dissociation.

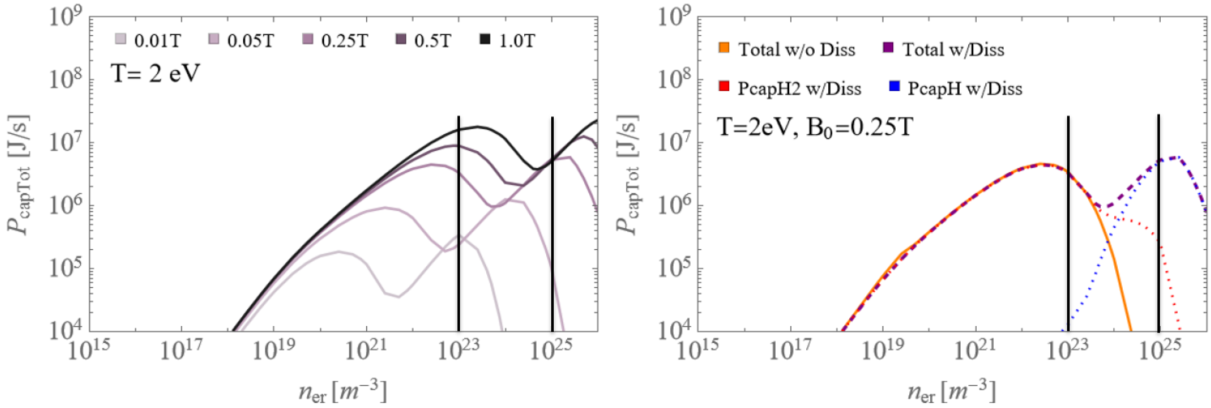

Figure 5.9: Parameter space identification for Figure 5.10 and5.11.

Figures 5.10 and 5.11 describe the densities of H2 and H in the control volume and surrounding areas for two different plasma densities under the same conditions. The black lines in Figure 5.9 visually indicate where in the parameter space these density distributions exist. The plasma density in Figure 5.10 is two orders of magnitude smaller than in Figure 5.11. The red and blue ovals represent the control volumes for the $H2$ and H capture regions respectively, as defined by Ψ^*. In Figure 5.10, the total power captured from the neutral stream is just past its first peak. Since the conditions shown are for lower temperatures, the first peak also corresponds to the maximum power captured from the $H2$ component of the neutral stream. In the density distribution for $H2$ shown on the left-hand side of Figure 5.10, there is a corresponding shadowing effect within most of the control volume, indicating that there is no more $H2$ in that region. However, the reaction front just in front of the shadowed region still falls inside of the control volume, indicating that there is still a population of $H2$ which will be ionized and captured into the plasma dipole.

In Figure 5.11 for the higher density case, the location of the reaction front for $H2$ has moved almost completely outside of the capture region for $H2$, which corresponds to only a very small amount of power being captured from the stream. Referring back to Figure 5.9 confirms that only a very small amount of power is being captured from the $H2$ component of the neutral stream. Physically, while the reactions are still taking place, the resulting ions are being deflected by the plasma dipole instead of captured. For the density of H, in Figure 5.11, there is again a shadowing region where there are no more neutrals. The reaction front is still within the blue control volume. While there is essentially no power being captured from the $H2$ population, the location of the reaction front indicates that there is power being captured from the H population. Looking back at Figure 5.9, this corresponds to the maximum power captured from the H population.

Figure 5.13 parameterizes the results discussed earlier in this section. Plotting the values of interest at the magnetic field strengths at which they occur provides a more quantitative look at the impact of dissociation on the power captured. While this is created for the nominal case where $T = 5eV$, the results can be extrapolated to the other cases observed.

In each of the subplots within Figure 5.13, either the plasma density, the power captured value, or the ratio between the two, at a physically significant location is plotted by magnetic field strength. There are two physically significant locations explored. The simpler of the two is the maximum. This location is where the maximum power capture occurs. The second location is the inflection point on the P_{in} curve. The inflection point represents a mode transfer in the state of the plasma dipole from being sustained by the injection of power into the plasma dipole to being sustained by the injection of power from the neutral stream itself. The locations where these shifts occur influences the implementation and feasibility of plasma aerocapture.

Figure 5.12 displays this breakdown for the nominal case with dissociation where $T = 5eV$ and $B_0 = 1T$. P_{in} is the sum of the injected power P_{inj} and $P_{cap,Tot}$. The value for P_{in} is dominated by the power injected into the plasma dipole until the plasma becomes dense enough to support itself. The transition point is marked in pink in Figure 5.12. The slope of the line at this location is the total power lost from the control volume. Shifts in this line demonstrate how the equilibrium split between P_{inj} and $P_{cap,Tot}$ changes. An outward shift places the equilibrium point lower on the P_{in} curve, where the impact of the injection regime is amplified. Shifting downward moves the equilibrium to a location where $P_{cap,Tot}$ dominated over P_{inj}. The gray point in Figure 5.12 denotes the maximum power captured.

At a temperature of $5eV$, these points and the corresponding plasma density and power values were collected by magnetic field strength. The subplots in Figure 5.13 display them.

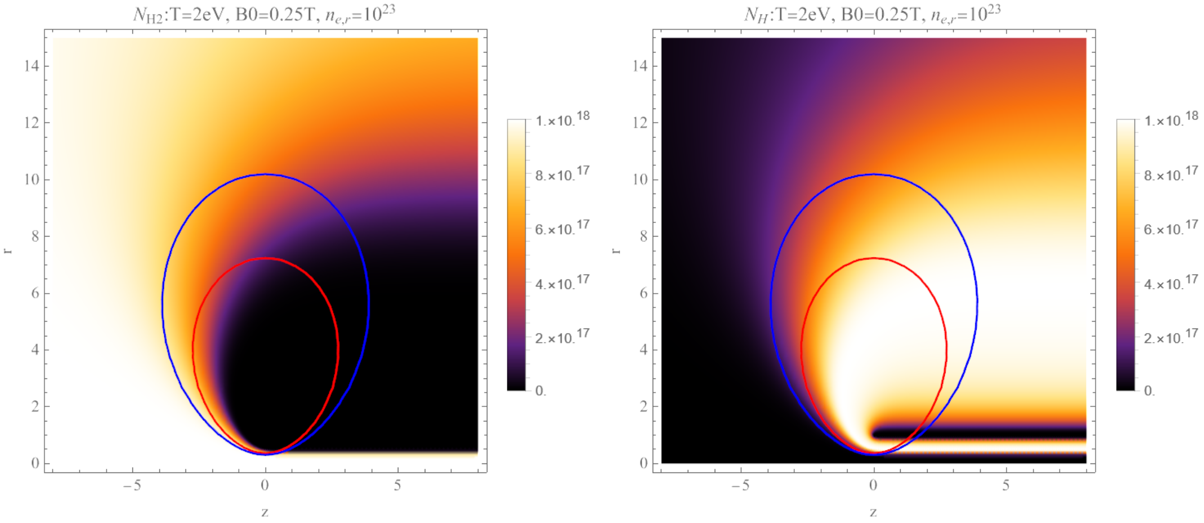

Figure 5.10: Density distribution for H2 (left) and H (right) for specified conditions at a plasma density of $n_{e,r} = 10^{23}$.

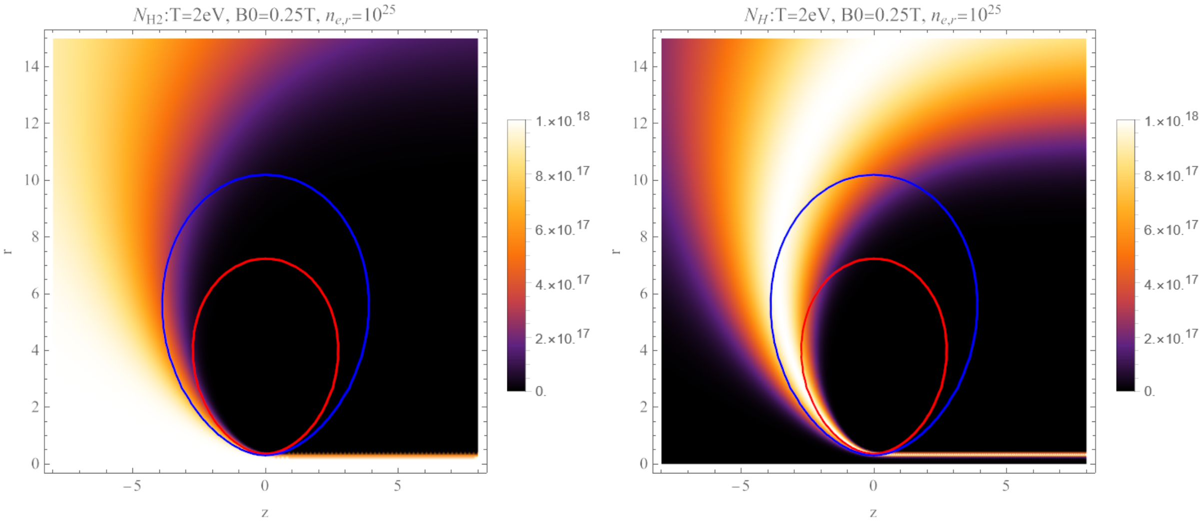

Figure 5.11: Density distribution for H2 (left) and H (right) for specified conditions at a plasma density of $n_{e,r} = 10^{25}$.

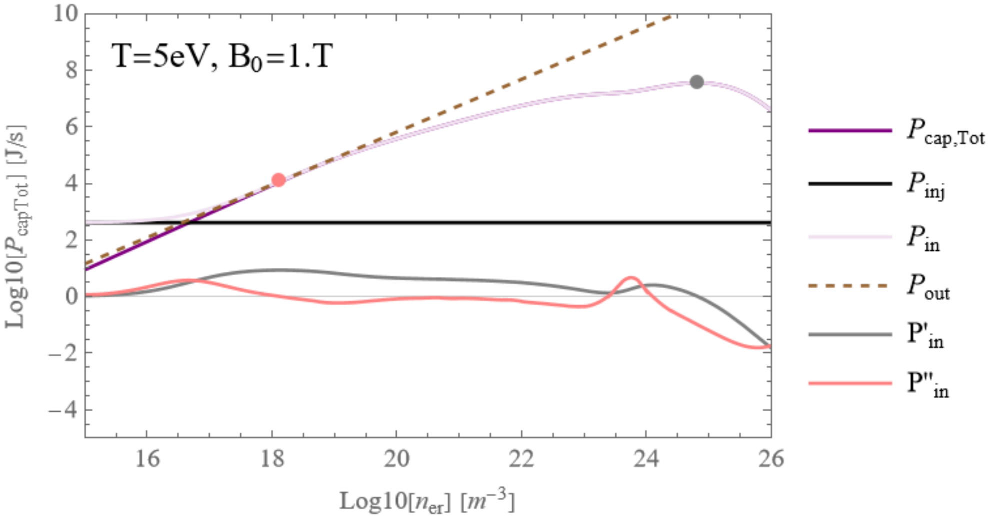

Figure 5.12: Total power captured, power injected, power in, power out, and the first and second derivatives of the power in as a function of plasma density.

Subplot a) displays the plasma density where the mode transition occurs. Overall, a lower plasma density is needed to transition between the regimes when dissociation is considered. In both cases, there is little variation in the plasma density of the transition between magnetic field strengths. Subplot b) looks at the power captured when the transition occurs. As before this value is greater for the case without dissociation. This means that when the MAC transitions to being self-sustaining, the power captured is smaller. The combination of subplots a) and b) result in subplot e), where the slope at the point of transition is plotted. Physically, the mode transfer is occurring at higher densities and powers for the case without dissociation because its range for power capture is more narrow than that of the case with dissociation. Since the inclusion of H widens the density range over which the power capture occurs, and because density and power captured scale in a linear fashion within this region, its mode transfer occurs at lower densities and resulting powers.

Subplot c) displays the density of the plasma when the power captured reaches its maximum. For both with and without dissociation, the density of the plasma at peak power captured increases with the magnetic field, with dissociation consistently providing for more maximum power captured at a given magnetic field. Since each particle captured brings with it a unit of kinetic energy, including H through dissociation, there are greater opportunities to capture power over just considering H2. For modeling MAC in general, this implies that accounting for dissociation will result in more power captured. This effect will be greater if the dissociated species is lighter compared to the atomic or molecular species because the corresponding capture area increases as the mass of the species decreases.

As outlined in [13] the practical application of MAC is dependent on its region of operation overlapping with a region within the atmosphere which allows for capture at a given planet. To find the flight envelope, the minimum u_∞ at which the plasma dipole is self-sustaining (ie. the point at which the mode transition occurs) is identified for a given n_∞ density. Then, that density is mapped onto a density map of the planet's atmosphere as a function of altitude. Since the mode transition occurs sooner with dissociation, this means that the flight envelopes are larger than predicted [13], implying that there is a wider range over which MAC can be applied.

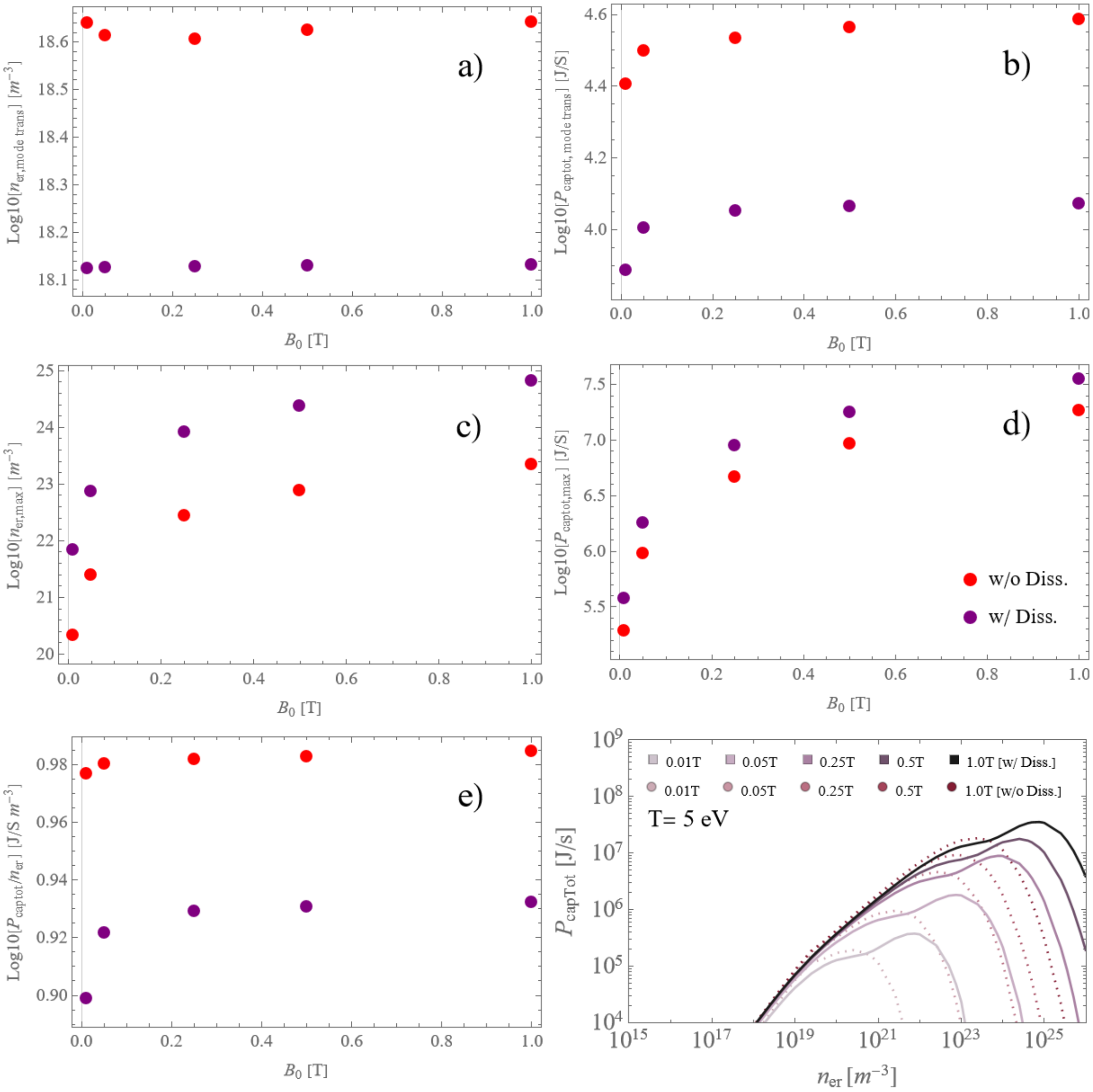

Figure 5.13: This set of plots parametrizes the minimum, maximum, and inflection values by the magnetic field for the case where $T = 5eV$, providing a clear view of how the results scale with magnetic field strength.

Chapter 6

CONCLUSION AND FUTURE WORK

MAC is a mission-enabling technology for the Ice Giants and Saturn and a mission-enhancing technology for Venus, Mars, and Titan. Its implementation has to potential to reduce cost through mass savings and to reduce risk through its ability to continuously vary drag and thus adapt to unforeseen elements within the atmosphere during capture. MAC

Previous analytical work has focused on implementing models for MAC which take into consideration electron impact charge exchange and ionization to determine the transfer of mass and energy between a neutral stream and a plasma dipole for a single species. Here, dissociation is considered in addition to electron impact charge exchange and ionization to further understand how mass and energy are transferred from the neutral stream to the plasma dipole. Findings indicate that including dissociation the mass and power transferred from the neutral stream to the dipole increases both the range over which the power can be transferred and the maximum amount of power being transferred. At lower temperatures, there is also a secondary maximum peak of power transfer which is a direct result of the dissociation. These shifts indicate that MAC becomes self-sustaining sooner than previously expected, which implies that the previously determined flight envelopes [13] for the regions across which MAC is viable are likely wider.

Future work could focus on expanding the model to self-consistently solve for mass and energy, utilizing these more detailed expressions for the power captured from the stream. In this way, the impact of differences in the density of n_∞ could be explored. Experimental campaigns to expand understanding of the entrainment of the neutrals into the plasma dipole could also be executed. In particular, spectrography could be employed to examine the distribution of species for a more detailed understanding of how the power transfer occurs.

BIBLIOGRAPHY

[1] Munk, M. M. and Moon, S. A., "Aerocapture technology development overview," *IEEE Aerospace Conference Proceedings*, 2008.

[2] Slough, J., Kirtley, D., and Pancotti, A., "Plasma Magnetoshell for Aerobraking and Aerocapture," *32nd International Electric Propulsion Conference*, 2011, pp. 9.

[3] Kirtley, D., "A Plasma Aerocapture and Entry System for Manned Missions and Planetary Deep Space Orbiters," *Phase I Final Report, MSNW LLC*, 2012.

[4] Kelly, C. L. and Little, J. M., "Energy and Mass Utilization during Drag-Modulated Plasma Aerocapture," *IEEE Aerospace Conference Proceedings*, Vol. March, 2019, pp. 1–10.

[5] James, B., Munk, M., and Moon, S., "AIAA 2003-4654 Aerocapture Technology Project Overview 39th Joint Propulsion Conference and Exhibit," *AIAA*, , No. July, 2003, pp. 1–4.

[6] Brandis, A. M. and Barnhardt, M. D., "New Developments in NASA's Entry Systems Modeling Project," *AIAA SciTech Forum*, , No. January, 2023, pp. 1–24.

[7] "Thousand times through the atmosphere of mars: Aerobraking the exomars trace gas orbiter," *15th International Conference on Space Operations*, , No. June, 2018, pp. 1–25.

[8] Nishimura, T. and Kawaguchi, J., "On the Guidance and Navigation of Japanese Spacecraft "HITEN", Double Lunar Swingy Demonstrator," *IFAC Proceedings Volumes*, Vol. 26, No. 2, 1993, pp. 777–782.

[9] Hall, J. L., Noca, M. A., and Bailey, R. W., "Cost-benefit analysis of the aerocapture mission set," *Journal of Spacecraft and Rockets*, Vol. 42, No. 2, 2005, pp. 309–320.

[10] Spilker, T. R., Adler, M., Arora, N., Beauchamp, P. M., Cutts, J. A., Munk, Michelle M., P. R. W., Braun, R. D., and Wercinski, P. F., "Qualitative Assessment of Aerocapture and Applications to Future Missions," *Journal of Spacecraft and Rockets*, Vol. 56, No. 2, 2019.

[11] Girija, A. P., Saikia, S. J., Longuski, J. M., Lu, Y., and Cutts, J. A., "Quantitative Assessment of Aerocapture and Applications to Future Solar System Exploration," *Journal of Spacecraft and Rockets*, Vol. 59, No. 4, 2022, pp. 1074–1095.

[12] Kirtley, D., "ISS Launched CubeSat Demonstration of Variable-Drag Magnetoshell Aerocapture: Phase I Final Report," *Phase I Final Report, MSNW LLC*, 2014.

[13] Kelly, C. L. and Little, J. M., "Performance Scaling and Mission Applications of Drag-Modulated Plasma Aerocapture," *36th International Electric Propulsion Conference*, 2019, pp. 1–18.

[14] Little, J. M. and Kelly, C. L., "Neutral flow interaction with a magnetic dipole plasma. I. Theory and scaling," *Physics of Plasmas*, Vol. 27, No. 11, 2020.

[15] Kelly, C. L. and Little, J. M., "Neutral flow interaction with a magnetic dipole plasma II. Global model," , No. August 2017, 2020.

[16] Kelly, C. L., Thoreau, P., and Little, J. M., "Experimental investigation of high velocity neutral flow interaction with a magnetized plasma," *Plasma Sources Science and Technology*, Vol. 31, No. 6, 2022.

[17] Larson, W. J. and Wertz, J. R., "Space Mission Analysis and Design," .

[18] London, H. S., "Change of Satellite Orbit Plane by Aerodynamic Maneuvering," *Journal of the aerospace sciences*, Vol. 29, No. 3, 1962, pp. 323–332.

[19] Roelke, E., Mcmahon, J. W., Braun, R. D., and Hattis, P. D., "Atmospheric Density Estimation Techniques for Aerocapture," *Journal of Spacecraft and Rockets*.

[20] Saikia, S. J., Millane, J., Lu, Y., Mudek, A., Arora, A., Witsberge, P., Hughes, K., Longuski, J. M., Spilker, T., Petropoulos, A., Arora, N., Cutts, J., Elliott, J., Sims, J., and Reh, K., "Aerocapture assessment for NASA Ice Giants Pre-Decadal Survey Mission Study," *Journal of Spacecraft and Rockets*, Vol. 58, No. 2, 2021, pp. 505–515.

[21] Girija, A. P., Saikia, S. J., Longuski, J. M., Bhaskaran, S., Smith, M. S., and Cutts, J. A., "Feasibility and performance analysis of neptune aerocapture using heritage blunt-body aeroshells," *Journal of Spacecraft and Rockets*, Vol. 57, No. 6, 2020, pp. 1186–1203.

[22] Putnam, Z. R. and Braun, R. D., "Drag-modulation flight-control system options for planetary aerocapture," *Journal of Spacecraft and Rockets*, Vol. 51, No. 1, 2014, pp. 139–150.

[23] Falcone, G., Williams, J. W., and Putnam, Z. R., “Assessment of aerocapture for orbit insertion of small satellites at Mars,” *Journal of Spacecraft and Rockets*, Vol. 56, No. 6, 2019, pp. 1689–1703.

[24] Munk, M. M., Braun, R. D., Landau, D., and Lyons, Daniel T., e. a., “An Assessment of Aerocapture and Applications to Future Missions,” *NASA Jet Propulsion Laboratory for Planetary Science Division Science Mission Directorate*, 2016.

[25] Dutta, Soumyo, e. a., “Aerocapture as an Enhancing Option for Ice Giants Missions,” *White Paper for the Planetary Science Decadal Survey*, 2023.

[26] Hancock, S. M., Moses, R. W., and Goyne, C., “Magnetoshell Aerocapture Performance Opportunities at Mars,” *2018 AIAA SPACE and Astronautics Forum and Exposition*, , No. September, 2018, pp. 1–14.

[27] Jackson, J. D., *Classical electrodynamics*, Wiley, New York, NY, 3rd ed., 1999.

[28] Trott, M., *The Mathematica GuideBook for Numerics*, Springer, 2006.

[29] Lockwood, M. K., “Neptune aerocapture systems analysis,” *Collection of Technical Papers - AIAA Atmospheric Flight Mechanics Conference*, Vol. 1, 2004, pp. 660–675.

[30] Janev, R., Reiter, D., and Samm, U., *Collision Processes in Low-Temperature Hydrogen Plasmas*, 2003.

[31] Lieberman, M. A. and Lichtenberg, A. J., *Principals of Plasma Discharges and Materials Processing*, John Wiley Sons, Inc., 2005.

[32] Barnett, C., “Collisions of H, H2, He and Li Atoms and Ions with Atoms and Molecules,” *Atomic Data for Fusion*, Vol. 1, 1990.

[33] Corrigran, S., “Dissociation of molecular hydrogen by electron impact,” *The Journal of Chemical Physics*, 1965.

[34] Riahi, R., Teulet, P., Lakhdar, Z. B., and Gleizes, A., “Cross section and rate coefficient calculations for electron impact excitation, ionisation and dissociation of the X 1g+, c 3Πu, a 3 g+, e 3u+ and B1u+ states of H2,” *European Physical Journal D*, Vol. 56, No. 1, 2010, pp. 61–66.

[35] Yoon, J. S., Song, M. Y., Han, J. M., Hwang, S. H., Chang, W. S., Lee, B., and Itikawa, Y., “Cross sections for electron collisions with hydrogen molecules,” *Journal of Physical and Chemical Reference Data*, Vol. 37, No. 2, 2008, pp. 913–931.

[36] Lu, Ping, a. C. C. J., Tigges, M. A., and Matz, D. A., "Optimal aerocapture guidance," *Journal of Guidance, Control, and Dynamics*, Vol. 38, No. 4, 2015, pp. 553–565.

[37] Moses, R. W., Cheatwood, F. M., Johnston, C. O., Green, J. S., Williams, R. A., and Austin, M., "Advanced Aerocapture System for Enabling Faster- Larger Planetary Science Human Exploration Missions," *Final Phase I Report: NASA Innovative Advanced Concepts*, , No. February 2021, 2021.

[38] Winske, D. and N., O., "Plasma expansion in the presence of a dipole magnetic field," *Physics of Plasmas*, Vol. 12, No. 7, 2005, pp. 1–12.

[39] Tseng, W. L., Johnson, R. E., and Ip, W. H., "The atomic hydrogen cloud in the saturnian system," *Planetary and Space Science*, Vol. 85, 2013, pp. 164–174.

[40] Surrey, E. and Holmes, A. J., "An ion species model for positive ion sources: I. Description of the model," *Plasma Sources Science and Technology*, Vol. 24, No. 1, 2015.

[41] Moses, Robert W., C. M. F., Christopher, J. O., Macheret, S. O., Bernard, P., Little, J., Austin, M., Aldrin, A., Green, J. S., and Williams, R. A., "New Magnetohydrodynamic (MHD) Lift Concept for More Efficient Missions to Mars and Neptune," *AIAA Science and Technology Forum and Exposition, AIAA SciTech Forum 2022*, 2022, pp. 1–14.

[42] Tabuchi, K., Sumitomo, R., Tanaka, K., and Fujino, T., "Numerical Analysis of Magnetohydrodynamic Flow Control in Mars Direct and Orbital Entries," *AIAA Science and Technology Forum and Exposition, AIAA SciTech Forum 2023*, , No. January, 2023, pp. 1–14.

[43] Steer, J., Collen, P. L., Glenn, A., Sopek, T., Hambidge, C., Doherty, L., McGilvray, M., Loehle, S., and Walpot, L., "Experimental Study of a Galileo Sub-Scale Model at Ice Giant Entry Conditions in the T6 Free-Piston Driven Wind Tunnel," *AIAA Science and Technology Forum and Exposition, AIAA SciTech Forum 2023*, , No. January, 2023, pp. 1–18.

[44] Ogilvie, J., Gildfind, D., Gollan, R., and Gibbons, N., "Feasibility of MHD Aerobraking for Use in Martian Atmospheric Entry," *AIAA Science and Technology Forum and Exposition, AIAA SciTech Forum 2023*, , No. January, 2023, pp. 1–25.

[45] Ingersoll, A. P. and Spilker, T. R., "A Neptune Orbiter with Probes Mission with Aerocapture Orbit Insertion," *NASA Space Science Vision Missions*, , No. 2000, 2008, pp. 81–114.

[46] Deshmukh, R. G., Spencer, D. A., and Dutta, S., "Investigation of direct force control for aerocapture at Neptune," *Acta Astronautica*, Vol. 175, No. September 2019, 2020, pp. 375–386.

[47] Coelho, J. and da Silva, M. L., "Aerothermodynamic analysis of Neptune ballistic entry and aerocapture flows," *Advances in Space Research*, Vol. 71, 2023, pp. 3408–3432.

[48] Lugo, R., Dutta, S., Matz, D., Johnson, B., Pensado, A., Roelke, E., Aguirre, J., and Powell, R., "Performance Analysis of SmallSat Aerocapture at Venus," *AIAA Science and Technology Forum and Exposition, AIAA SciTech Forum 2023*, , No. January, 2023, pp. 1–16.

[49] Kelly, C. L., "Magnetoshell Aerocapture: Advances Toward Concept Feasibility," *William E. Boeing Department of Aeronautics Astronautics*, 2018.

[50] Kelly, C. L., "Physics, Performance, and Applications of Plasma Aerocapture," *William E. Boeing Department of Aeronautics Astronautics*, 2021.

[51] Slough, J., "Plasma Magneto-Shell Aerocapture for Planetary Manned and Cargo Missions," *International Conference on Plasma Science*, 2022.

[52] Voronov, G., "A Practical Fit Formula for Ionization Rate Coefficients of Atoms and Ions by Electron Impact: Z=1-28," *Atomic Data and Nuclear Data Tables*, Vol. 65, 1997, pp. 1–35.

[53] McClure, G., "Charge Exchange and Dissociation of H+, H2+, and H3+ Ions Incident on H2 Gas," , No. 2, 1963, pp. 1–23.

[54] Errea, L. F., Illescas, C., MacÍas, A., Méndez, L., Pons, B., Rabadán, I., and Riera, A., "H+ + H2 collisions at low impact energies," *Journal of Physics: Conference Series*, Vol. 194, No. 10, 2009, pp. 1–2.

[55] Kimura, M., Igarashi, A., M., I., Y., I., Kitajima, M., Kusakabe, T., Moribayashi, K., Morishita, T., Motohashi, K., Pichi, L., Suzuki, K. D., Murakami, I., Kato, T., and Kato, M., "Report on Cross Section Data Compilation for Electron and Ion Collisions with Molecules of Hydrogen, Hydrogen Isotopes, Nitrogen, Hydrocarbons, Water and Carbon Dioxide," 2006.

[56] Nishimura, H., Danjo, A., and Sugahara, H., *Journal of the Physical Society of Japan*.

[57] Martin, A., "Reaction Cross Sections of Relevance to Hydrogen Plasmas CLM-R157," 1976.

[58] Martin, A. and Green, T., "Computations of Hydrogen Ion Species Produced in High Current Ion Sources CLM-R159," 1976.

[59] Erwin, D. A. and Kunc, J. A., "Rate Coefficients for Some Collisional Processes in High-Current Hydrogen Discharges," *IEEE Transactions on Plasma Science*, Vol. 11, No. 4, 1983, pp. 266–273.

[60] Buckman, S. J. and Phelps, A. V., "Vibrational excitation of D2 and H2 by low energy electrons," *The Journal of Chemical Physics*, Vol. 82, No. 11, 1985, pp. 4999–5011.

[61] Tawara, H., Itikawa, Y., Itoh, Y., Kato, T., Nishimura, H., Ohtani, S., Takagi, H., Takayanagi, K., and Yoshino, M., "Atomic Data Involving Hydrogens Relevant to Edge Plasmas," .

[62] Khakoo, M. A., Trajmar, S., McAdams, R., and Shyn, T. W., "Electron-impact excitation cross sections for the 3Σu+ state of H2," *Physical Review A*, Vol. 35, No. 7, 1987, pp. 2832–2837.

[63] Rescigno, T. N. and Schneider, B. I., "Electron-impact excitation of the b 3Σu+ state of H2 using the complex Kohn method: R dependence of the cross section," *Journal of Physics B: Atomic, Molecular and Optical*, Vol. 21, No. 22, 1988.

[64] Tawara, H., Itikawa, Y., Nishimura, H., and Yoshino, M., "Cross Sections and Related Data for Electron Collisions with Hydrogen Molecules and Molecular Ions," *Journal of Physical and Chemical Reference Data*, Vol. 19, No. 3, 1990, pp. 617–636.

[65] Sawada, K. and Fujimoto, T., "Effective ionization and dissociation rate coefficients of molecular hydrogen in plasma," *Journal of Applied Physics*, Vol. 78, No. 5, 1995, pp. 2913–2924.

[66] *University College London.*

[67] Stibbeyz, D. T. and Tennysony, J., "Near-threshold electron impact dissociation of H2 within the adiabatic nuclei approximation," *New Journal of Physics*, Vol. 1, 1998.

[68] Trevisan, C. S. and Tennyson, J., "Differential cross sections for near-threshold electron impact dissociation of molecular hydrogen," *Journal of Physics B: Atomic, Molecular and Optical Physics*, Vol. 34, No. 15, 2001, pp. 2935–2949.

[69] Capitelli, M., Celiberto, R., Esposito, F., Laricchiuta, A., Hassouni, K., and Longo, S., "Elementary processes and kinetics of H2 plasmas for different technological applications," *Plasma Sources Science and Technology*, Vol. 11, No. 3 A, 2002.

[70] Trevisan, C. S. and Tennyson, J., “Calculated rates for the electron impact dissociation of molecular hydrogen, deuterium and tritium,” *Plasma Physics and Controlled Fusion*, Vol. 44, No. 10, 2002, pp. 2217–2230.

[71] Riahi, R., Teulet, P., Lakhdar, Z. B., and Gleizes, A., “Cross-section and rate coefficient calculation for electron impact excitation, ionisation and dissociation of H2 and OH molecules,” *European Physical Journal D*, Vol. 40, No. 2, 2006, pp. 223–230.